Department of Precision and Microsystems Engineering

Topology optimization for suppression of vibrations in suspended structures and achieving dynamic global flatness

Chirag Garg

Report no.	: 2022.057
Coach	: Dr. Ir. Matthijs Langelaar, Ir. Arnoud Delissen
Professor	: Dr. Ir. Matthijs Langelaar
Specialisation	: Structural Optimization and Mechanics (SOM)
Type of report	: MSc Thesis
Date	: September 26, 2022

TOPOLOGY OPTIMIZATION FOR SUPPRESSION OF VIBRATIONS IN SUSPENDED STRUCTURES AND ACHIEVING DYNAMIC GLOBAL FLATNESS

Master of Science Thesis

by

Chirag Garg

in partial fulfilment of the requirements for the degree of Master of Science
at Delft University of Technology,
to be defended publicly on Monday, September 26, 2022 at 10:00.

Student number:	5346665	
Project duration:	July 19, 2021 to September 26, 2022	
Thesis committee:	Dr. Ir. Matthijs Langelaar	TU Delft
	Dr. Ir. Andres Hunt	TU Delft
	Ir. Arnoud Delissen	TU Delft
	Dr. Ir. Stan van der Meulen	ASML
	Dr. Ir. Emiel van de Ven	ASML

TU Delft Delft University of Technology

ASML

Abstract

In a high-precision system that performs measurements or tooling on a workpiece, alignment of the tool and workpiece is of prime importance. To prevent misalignment, which leads to a loss in accuracy and precision, unwanted vibrations in structures must be attenuated. Topology Optimization (TO) is evolving as a mature design tool that provides innovative designs beyond human creativity. This thesis focuses on developing and investigating TO methods for the limitation of response peaks on a flat surface for suspended structures. When optimizing for multiple excitation frequencies at multiple output points, the complexity of the problem increases, and the number of required constraints grows manifold. Thus, for a compact formulation, there is a need for aggregation of peaks in both dimensions, space, and frequency. Furthermore, the application requires the top surface of the suspended structure to remain flat during operation. In such a scenario, where a structure is excited harmonically, the dynamic deformations on the surface become key to quantifying surface flatness. The incorporation of dynamic flatness measures in TO framework is studied and implemented, and the results show that the proposed methods look promising.

Nomenclature

List of Symbols

$\mathbf{s}$	design density variable
s_{min}	minimum design variable density value
ρ	filtered design density variable
E	Young's modulus
ν	Poisson's ratio
ρ_{mat}	material density
r	filter radius
p_i	interpolation power
w	interpolation ratio
κ_i	stiffness element matrix scaling factor
μ_i	mass element matrix scaling factor
$\mathbf{K}_{el}$	stiffness element matrix
$\mathbf{M}_{el}$	mass element matrix
$\mathbf{K}$	system stiffness matrix
$\mathbf{M}$	system mass matrix
ω	frequency
η	hysteresis damping coefficient
$\mathbf{C}$	system damping matrix
$\mathbf{Z}$	system dynamic stiffness matrix
$\mathbf{u}$	system displacement vector
$\mathbf{b}$	input force vector
$\mathbf{c}$	output displacement vector
G	frequency transfer function
Ω	eigenfrequency
$\mathbf{\Phi}$	eigenvectors
$k_{1,x}$	spring 1 stiffness in x direction
$k_{1,y}$	spring 1 stiffness in y direction
$k_{2,x}$	spring 2 stiffness in x direction
$k_{2,y}$	spring 2 stiffness in y direction
V_f	volume fraction
J	number of frequencies
K	number of nodes
g_{upp}	transfer function upper limit
P_m	*p-mean*
P_n	*p-norm*
p	*p-norm* exponent
S_ω	input frequency set or band
S	sum of least squares fit residuals

List of Abbreviations

TO	Topology Optimization
FRF	Frequency Response Function
I/O	Input-Output
SIMP	Solid Isotropic Material with Penalization
MMA	Method of Moving Asymptotes
LSF	Least Squares Fit
MPF	Modal Participation Factor
MIMO	Multiple Input Multiple Output
MF	Metro(logy) Frame
IFM	InterFeroMeter

List of Figures

List of Tables

Contents

Chapter 1

Introduction

1.1 Background and Motivation

In a high-precision machine that performs measurements or tooling on a workpiece, alignment of the tool and workpiece is of prime importance. Misalignment can have various sources, such as static or dynamic mechanical loads. Such dynamic mechanical loads can cause unwanted vibrations in structures, leading to a loss of accuracy and precision. Structural vibration control has therefore been a hot topic in academics and various engineering industries like aerospace [1, 2], high-speed trains [3, 4], space optics [5] and other high-precision machinery [6]. The error margins for such machines are typically minimal.

In one such example of high precision machinery (explained further in Chapter 5), the error caused by vibrations must be in the order of nanometers or lesser. Currently, the design component, i.e., high accuracy positioning apparatus, is designed manually. However, manual designing in such a scenario becomes extremely strenuous considering the complexities of different domains such as static structural, mechanical dynamics, and thermal effects. These multi-domain requirements may also be dependent on each other, causing coupling.

Topology Optimization (TO) has emerged as a relief and is finding its way into various applications. TO is a design tool that iteratively computes a design in a given domain, a set of boundary conditions, and constraints to improve a particular performance metric [7]. In the given design domain, geometry can have any shape as long as it fulfills various requirements. TO often leads to innovative designs beyond human creativity, which are sometimes easy to understand but challenging to come up with.

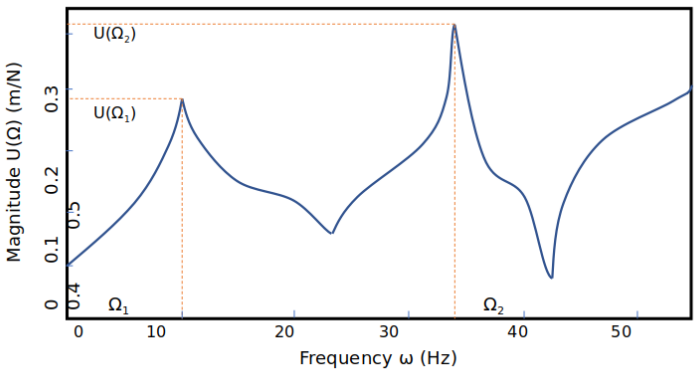

Figure 1.1: Frequency response function of a structure

Frequency response refers to the measure of the magnitude of the output signal (response) concerning a particular input signal (frequency). A **frequency response function (FRF)** is a complex transfer function used to quantify this response and express a frequency domain relationship between input and output signals, as shown in Figure 1.1. When a structure is harmonically excited at its eigenfrequencies (natural or resonant frequencies), it exhibits significantly high-frequency responses. It is possible to mitigate such high vibration levels by designing structures with their eigenfrequencies adjusted to avoid the working frequency bands of the machine. Various methods have been developed and presented to maximize fundamental and higher-order eigenfrequency to extend the operating excitation range of frequency [8]. The problem of maximizing the difference between two adjacent eigenfrequencies of a beam [9, 10] or obtaining eigenfrequencies close to prescribed frequencies [11] have also been presented. An overview of available approaches for optimizing eigenfrequencies has also been presented [12].

A structure may be subject to various excitation frequencies scattered over different frequency domains in a dynamic mechanical system. A structure's eigenfrequencies may lie in any of these bands, and in order to avoid resonance, the resonant response needs to be optimized, and response at several other frequencies needs to be considered. An often used method to avoid or limit structural resonance is to discretize the frequency range into lots of frequency points and then minimize the vibrational amplitude of a point or some subdomains of the structure under steady-state harmonic loading with prescribed excitation frequency and amplitude [13, 14, 15, 16, 17]. Some research papers have also considered multi-objective optimization of structural compliance and eigenfrequency [18, 19]. Various methodologies for minimization of vibrational performance measures have been explored [20]. Some physical and mathematical characteristics of dynamic compliance have been presented, showing that it is inadequate to use as an objective function. Some other vibration measures, such as active input power, i.e., net power dissipated by a damped vibrating system, were suggested, which more adequately represent the dynamic behavior of structures.

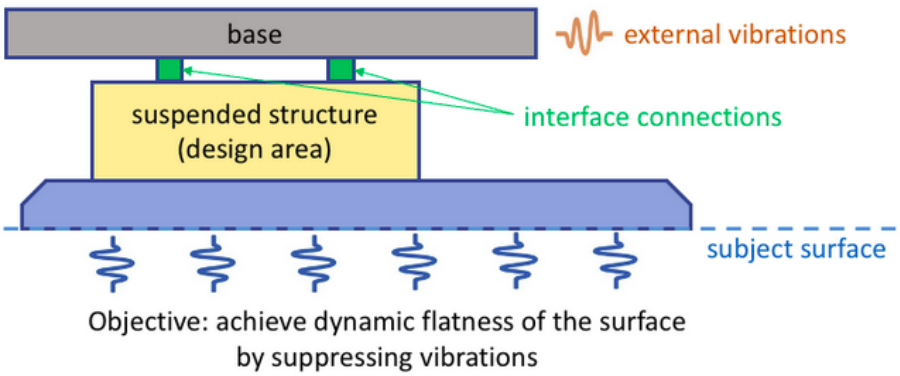

Figure 1.2: Non-collocated I/O system where vibrations originating from the base and propagating through interface connections need to be suppressed on the surface to achieve dynamic flatness

Besides the eigenfrequencies of the structure and the spectrum of input excitations, the dynamic behavior of a structure is also determined by the geometric location of input load and output point(s) where vibrations need to be minimized. A structure suspended from a base through some interface connections, subject to vibrations propagating through these interface connections, is shown in Figure 1.2. This is a **non-collocated input-output (I/O) system**, where external vibrations propagating through interface connections must be minimized at some user-defined point(s) on a flat surface.

Vibration levels must be restricted at multiple points over the entire surface for multiple output cases. Applying individual constraints for each point (node) on this surface would lead to a lengthy TO formulation. It becomes difficult for the optimizer to handle many constraints together,

increasing computational time. In addition, when optimizing for multiple excitation frequencies, implementing an individual constraint per frequency again leads to an extensive formulation and significant computational times. When both problems are considered together, i.e., optimizing for multiple frequencies at multiple points, the problem's complexity increases and the number of constraints required grows manifold. Thus, peaks must first be aggregated in both dimensions, space and frequency, and then constrained for a compact formulation. Additionally, the stiffnesses of the interface connections between the structure and the base also influence the dynamic characteristics of the system, especially the suspension modes. Optimization of these stiffnesses also becomes crucial to such design problems.

Furthermore, the application requires the top surface of the apparatus to remain flat during operation (Chapter 5). **Surface flatness** is defined as the deviation in the height of the surface relative to a reference plane over short distances in a local area [21]. When surface flatness is considered over a larger scale, such as the entire surface, it is termed global flatness, as illustrated in Figure 1.3. Global flatness for dynamical systems (e.g., wafer tabletop, deformable mirrors) has been chiefly associated with control systems for flatness correction using sensors and actuators [22, 23]. In such a scenario, where a structure is excited harmonically, the dynamic deformations on the surface become key to quantifying surface flatness. Dynamic global flatness is a new concept that has not yet found its way in TO context to the best of our knowledge. In this thesis, the incorporation of dynamic flatness measures in TO framework is studied and implemented for harmonically excited structures.

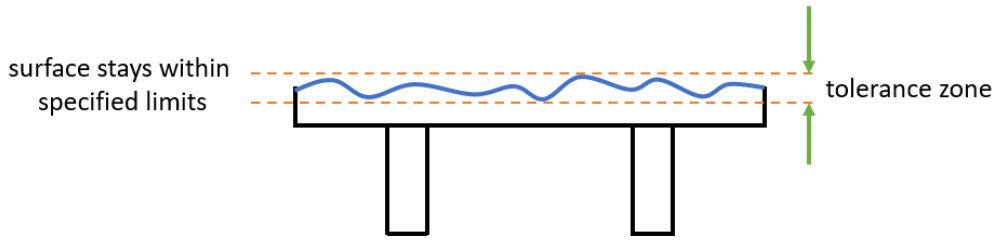

Figure 1.3: Surface flatness: the measure of deviations in the height of the surface

1.2 Research goals and Approach

As per the complexities discussed in the previous section, the objective of this MSc thesis can be summarized in the form of research goals as follows:

1. Development and investigation of TO methods for limitation of dynamic response on a flat surface for suspended structures, i.e., non-collocated I/O systems
2. Development and incorporation of global flatness measures in TO framework for a dynamical mechanical system

In order to gain insights into the above mentioned research topics, we first explore the fields of TO in mechanical dynamics and seek state-of-the-art techniques to solve such industrial problems (Chapter 2). With a careful choice of methodologies and strategies presented, we look to improve the dynamic performance characteristics of the system (Chapter 3). A base benchmark design has been selected for comparison with generated designs as we build more complexities in the model. Global flatness for dynamical mechanical systems is introduced and implemented in TO framework (Chapter 4). Chapter 5 covers the case study, already briefly mentioned, of designing the high accuracy positioning apparatus. We conclude in the final Chapter 6 with some discussion on the results achieved and future recommendations.

Chapter 2

Topology Optimization

Topology Optimization (TO) [24] is a material distribution method used to optimize a material layout with a given design domain, set of boundary conditions, and constraints in order to improve a particular performance metric. This performance metric, also known as the objective function, can be physical quantity like mean compliance, peak stress, deflection, eigenfrequency, dynamic response, etc., which can be maximized or minimized as per the requirements.

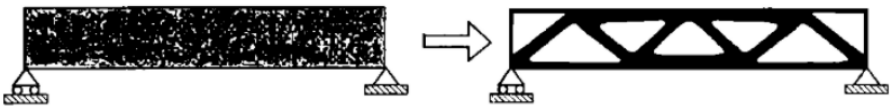

Figure 2.1: Topology Optimization

TO optimizes a specific design domain by determining the number, shape, and location of holes and, thus, the connectivity of the domain structure. Known parameters during the process include applied loads, support conditions, the volume of the structure, and the design constraints, which in turn are used to determine the physical size and shape of the design structure.

2.1 Density based method

The density-based approach [7] is one of the most widely used methods in TO. In this approach, the given design domain is discretized into small elements, with each element recognized by a density variable. The mechanical properties of the finite element model are dependent on these density variables. Each element in the design space is a material point (density 1) or a void (density 0), and the optimization problem is converted from a discrete variable into a continuous problem. **SIMP (Solid Isotropic Material with Penalization)** [25] makes use of a penalty factor that steers the solution towards discrete 0-1 values. The intermediate density values which are unfavorable are penalized by choosing a penalty power factor, p_i, and thus forming a black and white design with points being attributed to either density 0 or 1. To avoid the singularity of the stiffness matrix, instead of choosing zero as the minimum density of a void, a non-zero minimum value, s_{min} is chosen. This ensures that the minimum value of the density of an element is independent of the penalization factor. The SIMP method is further modified wherein the element stiffness matrix is scaled using a combination of a linear term (weighted by w) and a part with exponent p_i [26].

$$\kappa_i = (1-w)\rho_i^{p_i} + w\rho_i \qquad \text{and} \qquad \mu_i = \rho_i \tag{2.1}$$

where κ_i and μ_i are the scaling factors for stiffness and mass element matrices, respectively.

2.2 Method of Moving Asymptotes

The Method of Moving Asymptotes (MMA) [27] is a method for non-linear programming in structural optimization. In each iteration step, a convex sub-problem is generated and solved based on sensitivity information at that iteration point and also some iteration history. These sub-problems are controlled by 'moving asymptotes,' which are instrumental in stabilization and speeding up the process. A major advantage of using MMA is that the approximations generated are separable and convex in nature. MMA may be a bit slower than the Optimality Criteria method but is better suited to handle more complicated problems involving several constraints, where it has shown excellent convergence probabilities.

2.3 Sensitivity analysis

Sensitivity Analysis is termed as understanding the effect of some independent variables on some dependent variables or, as known in TO, calculation of derivatives of displacements with respect to design variables. The most common method used for sensitivity analysis is the **adjoint method**, where a Lagrangian is used to eliminate sensitivities of state variables which reduces computational time. For a constraint equation, the adjoint calculation is derived by adding Lagrange multipliers. By choosing the adjoint vector λ correctly, we can cause the state sensitivities $\frac{\mathrm{d}u}{\mathrm{d}x}$ to drop out.

$$\begin{aligned} \mathcal{L}(x,u) &= f(x,u) + \lambda^T g(x,u) \\ \frac{\mathrm{d}\mathcal{L}}{\mathrm{d}x} &= \frac{\partial f}{\partial x} + \frac{\partial f}{\partial u}\frac{\mathrm{d}u}{\mathrm{d}x} + \lambda^T\Big(\frac{\partial g}{\partial x} + \frac{\partial g}{\partial u}\frac{\mathrm{d}u}{\mathrm{d}x}\Big) \\ &= \frac{\partial f}{\partial x} + \lambda^T\frac{\partial g}{\partial x} + \Big(\frac{\partial f}{\partial u} + \lambda^T\frac{\partial g}{\partial u}\Big)\frac{\mathrm{d}u}{\mathrm{d}x} \\ \therefore \frac{\mathrm{d}\mathcal{L}}{\mathrm{d}x} &= \frac{\partial f}{\partial x} + \lambda^T\frac{\partial g}{\partial x} \qquad \text{s.t.} \qquad \frac{\partial f}{\partial u} + \lambda^T\frac{\partial g}{\partial u} = 0 \end{aligned} \tag{2.2}$$

2.4 Density filter

To ensure mesh in-dependence in density based TO, various filters have been devised. Density filters redefine each element density as a weighted average of densities of mesh-independent neighboring elements [28]. Thus the stiffness of a particular element would now depend on the density of all elements in the neighborhood of that particular element. This leads to a smoothing of the stiffness fields and refinement of the density variable. The variations in the density fields that appear as grey scale regions can later be penalized by SIMP providing a black and white design.

2.5 Dynamic modelling

Most precision mechanisms are composed of rigid bodies connected through some interface connections. Such mechanisms are prone to errors in accuracy and precision due to the transfer of vibrations from one rigid body part to another. The system's capability to transmit motion from one area to another, both inside the body and between connected bodies, is known as transmissibility. Optimizing the transmissibility transfer function becomes imperative to limit vibrations for such suspended structures or mechanisms.

In this work, research is focused on structures suspended from a base through some interface connections. As shown in Figure 1.2, non-collocated I/O systems are those where input and output are located at different places, i.e., vibrations arising from the base propagate through the interface connections (input) and have to be optimized at some other specified user-defined points (output). For such a system, we need a model suited for TO to understand the various factors involved in choosing a suitable objective and constraint functions. With an initial focus on implementation and investigation, the problem was studied in 2D (IMSYS-3D developed software in Python). Later, the developed methodologies were implemented in 3D (IMSYS-3D developed software in C++) for the case study in Chapter 5.

We build a model with the interface connections modeled as two springs, as shown in Figure 2.2. We take the top layer as a non-design layer (with density variable $\mathbf{s}_{\text{top}} = 1$) since we want that domain to be completely solid and indicate a continuous flat surface where vibrations need to be minimized. The design variables, $\mathbf{s}$, are first filtered with a spatial density filter to avoid checkerboarding and control the length scale of the design, yielding filtered design variables ρ. To compel the optimizer to a clear black and white design, the gray scale regions are penalized by SIMP (Equation 2.1).

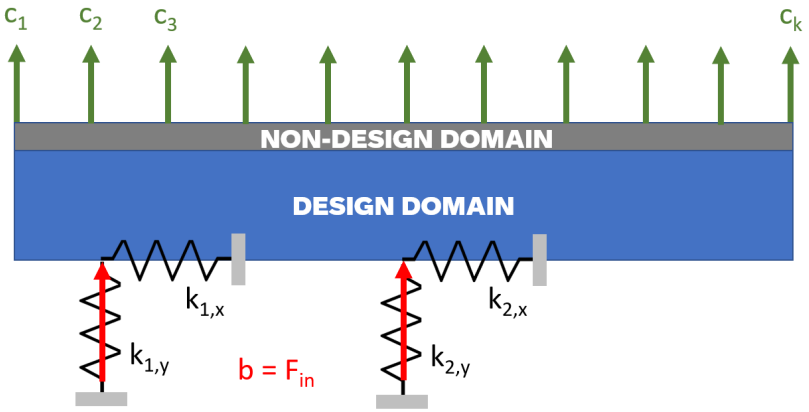

(a) Schematic of model

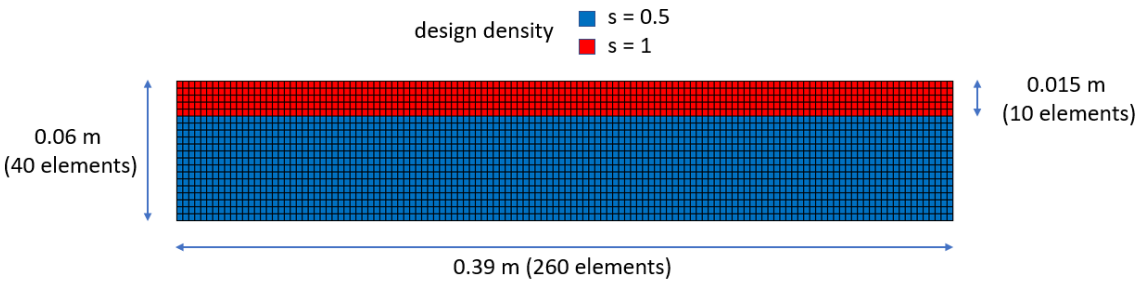

(b) Mesh of model

Figure 2.2: Model: TO of non-collocated I/O systems

For the discretization, we use bi-linear quadrilateral finite elements, a 2 x 2 Gaussian quadrature, and assume a plane strain condition. The stiffness element and the mass element matrices ($\mathbf{K}_{el}$ and $\mathbf{M}_{el}$) are scaled using scaling factors (κ_i and μ_i) to assemble system stiffness and mass matrices ($\mathbf{K}$ and $\mathbf{M}$) using scaling factors as follows:

$$\mathbf{K} = \sum_{i}^{n_{el}} \kappa_i \mathbf{K}_{el}^{(i)} \qquad \text{and} \qquad \mathbf{M} = \sum_{i}^{n_{el}} \mu_i \mathbf{M}_{el}^{(i)} \tag{2.3}$$

The dynamic equation of motion for this system with multiple degrees of freedom (DOFs) can be written in the form as follows:

$$\mathbf{M}\ddot{\mathbf{U}}(t) + \mathbf{C}\dot{\mathbf{U}}(t) + \mathbf{K}\mathbf{U}(t) = \mathbf{F}(t) \tag{2.4}$$

where $\mathbf{M}$, $\mathbf{C}$ and $\mathbf{K}$ are the mass, damping and stiffness matrices respectively, $\mathbf{U}(t)$ is the row vector containing all DOFs, and $\mathbf{F}(t)$ contains all external forces. $\mathbf{U}(t), \dot{\mathbf{U}}(t)$, $\ddot{\mathbf{U}}(t)$ and $\mathbf{F}(t)$ are time-dependent and can be expressed in harmonic form as shown:

$$\begin{aligned} \mathbf{U}(t) &= \mathbf{u}e^{\iota\omega t} \\ \dot{\mathbf{U}}(t) &= \iota\omega\mathbf{u}e^{\iota\omega t} \\ \ddot{\mathbf{U}}(t) &= -\omega^2\mathbf{u}e^{\iota\omega t} \\ \mathbf{F}(t) &= \mathbf{f}e^{\iota\omega t} \end{aligned} \tag{2.5}$$

We employ hysteretic damping, a form of structural damping which is proportional to displacement. A damping coefficient η is used to create a complex stiffness [29].

$$\mathbf{C} = \frac{\mathbf{K}\eta}{\omega} \tag{2.6}$$

For dynamic response, we use a steady-state system with harmonic inputs and outputs. Equation 2.4 can be substituted with harmonic forces and displacements to obtain the discretized N-dimensional frequency domain system of equations.

$$\begin{aligned} \Big(\mathbf{K}(\mathbf{1} + \iota\eta) - \omega^{\mathbf{2}}\mathbf{M}\Big)\mathbf{u}(\omega) &= \mathbf{b}q(\omega) \\ y(\omega) &= \mathbf{c}^{\mathrm{T}}\mathbf{u}(\omega) \end{aligned} \tag{2.7}$$

where $\mathbf{u}$ denotes the state vector capturing the displacements and deformations of the entire structure. The input vector $\mathbf{b}$ and output vector $\mathbf{c}$ describe the spatial distribution and direction of the unit input force and the observed unit displacement, respectively, as shown in Figure 2.2a.

This can further be written into a complex frequency-dependent transfer function $G(\omega)$, denoting transmission between the input force and output displacement.

$$G(\omega) = \frac{y(\omega)}{q(\omega)} = \mathbf{c}^{\mathrm{T}}\Big(\mathbf{K}(\mathbf{1} + \iota\eta) - \omega^{\mathbf{2}}\mathbf{M}\Big)^{-1}\mathbf{b} = \mathbf{c}^{\mathrm{T}}\mathbf{Z}(\omega)^{-1}\mathbf{b} \tag{2.8}$$

where $\mathbf{Z}(\omega)$ is the complex symmetric $N \times N$ frequency dependent dynamic stiffness matrix. The magnitude of $G(\omega)$ is used to obtain the amplification of harmonic amplitudes from input to output.

Hysteretic damping does not affect the frequencies at which the peak amplitudes occur, so eigenfrequencies of an undamped system can directly be used in our formulation. The undamped eigenfrequencies Ω_i and eigenvectors $\boldsymbol{\phi}_i$ of the system can be calculated by solving the general eigenvalue problem

$$\mathbf{K}\boldsymbol{\phi_i} = \Omega_i^2\mathbf{M}\boldsymbol{\phi_i} \quad \forall \quad i = 1, ..., n \tag{2.9}$$

The eigenvectors $\mathbf{\Phi} = [\boldsymbol{\phi_1}, \boldsymbol{\phi_2}, ..., \boldsymbol{\phi_n}]$ are mass orthonormalized as $\mathbf{\Phi}^{\mathrm{T}}\mathbf{M}\mathbf{\Phi} = \mathbf{I}$.

The physical properties and variables used in the optimization problems are summarized in Table 2.1.

Table 2.1: Physical properties and variables used in the optimization problems

Parameter	**Description**	**Value**
E	Young's modulus	90 GPa
ν	Poisson's ratio	0.24
ρ_{mat}	Density	2530 $\mathrm{kg\,m^{-3}}$
η	Hysteretic damping coefficient	10^{-3}
s_{min}	Minimum design value	10^{-3}
n	Number of eigenfrequencies considered	6
r	Filter radius	2 elements
w	Interpolation ratio	0.9
p_i	Interpolation power	4
p	p-norm exponent	20
$k_{1,x}$	Spring 1 stiffness in x direction	1.74×10^6 $\mathrm{N\,m^{-1}}$
$k_{1,y}$	Spring 1 stiffness in y direction	2.70×10^8 $\mathrm{N\,m^{-1}}$
$k_{2,x}$	Spring 2 stiffness in x direction	5.00×10^8 $\mathrm{N\,m^{-1}}$
$k_{2,y}$	Spring 2 stiffness in y direction	5.00×10^8 $\mathrm{N\,m^{-1}}$
	Mesh size	260×40

Chapter 3

Vibration Suppression

This Chapter focuses on the suppression of vibrations for non-collocated I/O cases. We begin by understanding the eigenmodes of our model and the factors influencing its eigenfrequencies. This is succeeded by discussing possible objective functions suitable for such problems. We formulate the TO problem based on aggregation techniques in both the spatial and frequency domain. We conclude the Chapter with a summary of inferences drawn from each section.

3.1 Suspension modes and dynamic eigenmodes

The structure model's (Figure 2.2) first six eigenmodes for uniform volume fraction (V_f) 0.5 can be seen in Figure 3.1. Taking the first three eigenmodes, which are **suspension modes** and the next three **dynamic eigenmodes**, we study the parameters influencing its eigenfrequencies. Suspension modes are the low-frequency rigid body modes that exhibit some internal deformation at the eigenfrequency of the suspension [30]. Analytical validation of eigenfrequency values can be found in Appendix A.

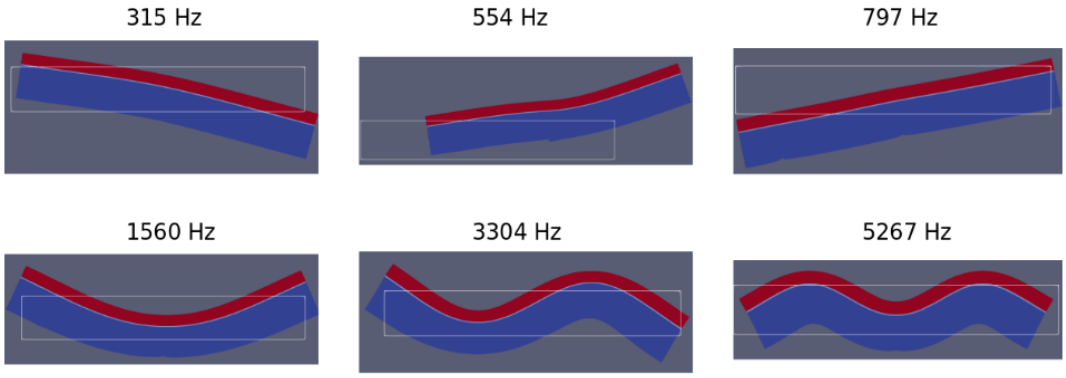

Figure 3.1: First six eigenmodes of model with uniform $V_f = 0.5$

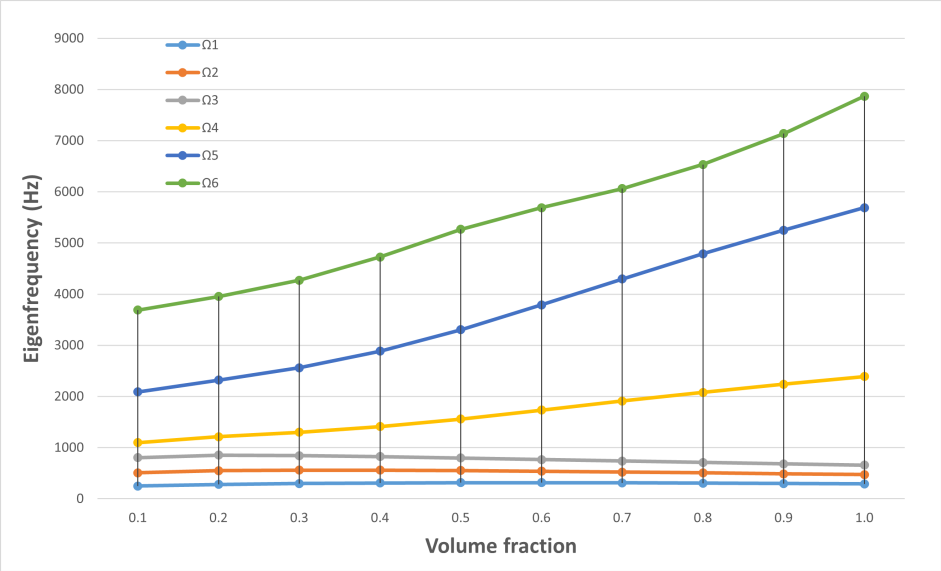

Figure 3.2: Variation in eigenfrequencies of model with respect to V_f

The first three eigenmodes are majorly suspension modes because of the springs. These eigenfrequencies are defined by the mass of the structure and the stiffness of interface connections. In contrast, the following three dynamic eigenmodes' eigenfrequencies are defined by the mass and stiffness of the structure as a whole. Variation in eigenfrequencies of the model with respect to V_f is shown in Figure 3.2. The first three eigenfrequencies decrease when we increase the V_f from 0.1 to 1. This can be attributed to an increase in mass while the stiffness of the interface connections remains the same, which ultimately leads to lowering these eigenfrequencies. However, the following three dynamic eigenmodes can be observed to have increased eigenfrequencies owing to a comparably more significant increase in the stiffness of the structure (depending on the value of penalty factor in SIMP) than the mass of the structure.

3.2 Optimization problem formulation

As per discussions in Section 2.5, probable **objective functions** under consideration for such TO problems are:

1. Static compliance minimization
2. Transfer function minimization
3. Eigenfrequency maximization
4. Weight minimization

Since we aim to keep a flat surface, all nodes on the top surface of the structure need to be considered. In such cases, calculating static compliance at each node and forming a weighted objective function may seem appropriate. However, it seems logical to focus on dynamic compliance-based functions instead of static compliance to influence the dynamic characteristics of the structure. A challenge faced with non-collocated I/O systems is that transfer function minimization is not feasible because to minimize the transfer function, the optimizer would compel the design to not form a connection between the input loading and output displacement points. This is because it would prevent the input forces from acting on the structure, preventing deformations at the output location points. This can be solved by making use of static compliance constraints. However, incorporating transfer functions as a weighted objective function seems irrational. Considering transfer functions as constraints imparts meaning to our problem wherein we optimize our design

to suppress vibrations below a prespecified limit. Therefore, transfer functions in this work are treated as constraints.

A reasonable choice for eigenfrequency maximization is based on **mean eigenvalue** [11]:

$$f(\mathbf{s}) = \left(\sum_{i=1}^{n} \frac{1}{\Omega_i(\mathbf{s})} \right) \tag{3.1}$$

where n is the total number of eigenmodes considered. The interface connections control the suspension modes of the structure, which in turn influence its first three eigenfrequencies. The influence of suspension modes and dynamic eigenmodes on the mean-eigenvalue objective function is investigated in Appendix B. Suspension modes must be included in the objective function to ensure structure formation relevant to boundary conditions. The number of flexible modes to be included would depend on the highest frequencies of excitations the system is subjected to. In this work, three suspension modes and three flexible modes are considered in the objective function. We now focus on the parameters influencing optimization of suspension mode frequencies and flexible eigenfrequencies. Three optimization formulations are considered:

Table 3.1: Optimization formulations:
1. Eigenfrequency maximization with volume constraints
2. Eigenfrequency maximization (normalized) with volume constraints
3. Eigenfrequency maximization without volume constraints

Case	**Objective**	**Volume**	$\boldsymbol{\Omega_1}$	$\boldsymbol{\Omega_2}$	$\boldsymbol{\Omega_3}$	$\boldsymbol{\Omega_4}$	$\boldsymbol{\Omega_5}$	$\boldsymbol{\Omega_6}$
	Ω_{initial} (itr. 1)	$V_{f,\text{initial}} = 0.50$	315 Hz	554 Hz	797 Hz	1560 Hz	3304 Hz	5267 Hz
1	$\sum_{i=1}^{n} \frac{1}{\Omega_i}$	$0.50 < V_f < 0.60$	439 Hz	626 Hz	802 Hz	2275 Hz	4253 Hz	5639 Hz
		% increase	39%	13%	01%	46%	22%	07%
2	$\sum_{i=1}^{n} \frac{\Omega_{\text{initial}}}{\Omega_i}$	$0.50 < V_f < 0.60$	422 Hz	615 Hz	850 Hz	2743 Hz	5093 Hz	6920 Hz
	(normalized)	**% increase**	34%	11%	07%	76%	54%	31%
3	$\sum_{i=1}^{n} \frac{1}{\Omega_i}$	$V_{f,\text{final}} = 0.19$	457 Hz	755 Hz	1029 Hz	2068 Hz	3286 Hz	3819 Hz

A summary of results for three optimization formulations with different objective functions and volume constraints is tabulated in Table 3.1. The optimized designs obtained have been shown in Figure 3.3. It can be seen from the results obtained that the higher eigenfrequencies ($\Omega_4, \Omega_5, \Omega_6$) increase by a greater extent in case 2 because of normalization. This is because in case 1, the objective function consists of the reciprocals of the eigenfrequencies, due to which higher eigenfrequencies have a comparatively lower contribution in the objective function as compared to the low frequencies ($\Omega_1, \Omega_2, \Omega_3$). After normalization with respect to the initial values (i.e., iteration 1 values), all eigenfrequencies have equal contributions in the objective function for the first iteration. Therefore, higher eigenfrequencies increase by a more significant margin due to normalized eigenfrequencies. This effect could be seen in obtained optimized designs. The design in case 2 (Figure 3.3b) was observed to have more triangular and web-like structures as compared to the optimized design of case 1 (Figure 3.3a). Such trusses are associated with stability and strength as energy is distributed in a much more balanced manner. This is in accordance with the higher eigenmodes requiring more rigidity and stiffness due to increased corresponding eigenfrequencies.

(a) Case 1: Eigenfrequency maximization with volume constraints

(b) Case 2: Eigenfrequency maximization (normalized) with volume constraints

(c) Case 3: Eigenfrequency maximization without volume constraints

Figure 3.3: Optimized designs obtained from formulations shown in Table 3.1

Also, it must be understood that since the higher eigenfrequencies ($\Omega_4, \Omega_5, \Omega_6$) correspond to the flexible modes, they depend on both the mass and stiffness of the system, which makes their optimization highly flexible. On the other hand, the low eigenfrequencies ($\Omega_1, \Omega_2, \Omega_3$), which correspond to the suspension modes, are highly dependent on the stiffness of interface connections which are not very flexible in the optimization. This comparatively restrains their optimization unless the spring stiffnesses are also provided as variables to the optimizer (which is explored in Section 3.5). For now, we will restrict our study to optimizing response at frequencies lying in the range of higher (flexible) eigenfrequencies only.

It was observed that the lower volume constraint was active for both case 1 and case 2, which meant that the optimizer was pushing towards lower V_f designs. The optimized design of eigenfrequency maximization without any volume constraints (case 3) can be seen in Figure 3.3c with a resulting V_f of 0.19. The design depicts clear truss formation to achieve maximum stiffness. It was noticed that the optimizer pushes towards higher V_f structures when only flexible modes are included in the objective function. However, with the inclusion of suspension modes, the optimizer pushes the design towards lower V_f since eigenfrequencies are inversely proportional to the mass of the structure (Appendix B). The mass of the structure plays a pivotal role in deciding the eigenfrequencies of suspension modes. So, weight minimization is implicitly achieved in the mean eigenvalue objective function when suspension modes are included. As for the choice of enforcing a V_f constraint, it is quite subjective and would vary across applications. In this report, most formulations involve the implementation of V_f constraints as it results in more evident designs which are comparatively more rational and easier to comprehend.

Some multi-objective formulations, including the mean-eigenvalue function and transfer function, were investigated with different weighing fractions in Appendix C. It was observed that both functions act against each other; while the mean-eigenvalue function promotes structure formation, the transfer function prevents structure formation between I/O points so that the deformations can be minimized.

In this thesis, application of response constraints has been studied with mean-eigenvalue as objective function along with enforcing volume constraint. This leads to the following optimization problem which is considered throughout this chapter:

$$\begin{aligned} \min_{\mathbf{s}} \quad & \left(\sum_{i=1}^{n} \frac{1}{\Omega_i(\mathbf{s})} \right) \\ \text{s.t.} \quad & \left| G_k(\omega_j, \mathbf{s}) \right| \leq g_{\text{upp}}(\omega_j) \quad \forall \quad j = 1, ..., J, \quad k = 1, ...K \\ & V_f \geq 0.5 \\ & s_{\min} \leq \mathbf{s} \leq 1 \end{aligned} \tag{3.2}$$

where $\left| G_k(\omega_j, \mathbf{s}) \right|$ represents the response magnitude at any node k and at any excitation frequency ω_j. g_{upp} represents the upper limit of the transfer function for specified excitation frequency. For simplicity, we abbreviate the frequency response transfer function expression from $\left| G_k(\omega_j, \mathbf{s}) \right|$ to $G_k(\omega_j)$. The two indices, j and k, clearly show the rapid growth in the number of constraints when multiple nodes and frequencies are considered. This calls for aggregation strategies to aggregate constraints in both the spatial and frequency dimensions.

The objective function value is scaled to 100 for the first iteration. The constraints are scaled such that their first iteration values lie from 1 to 10. The termination condition for all optimizations was convergence at design variable tolerance of 5×10^{-4}. It must be further understood that, as per our application requirements, the values obtained by our objective function are not as salient as the obedience of constraints. The objective function for our formulation is vital in ensuring that a structure is formed, but the constraints provide purpose and solution to our problem.

3.3 Aggregation in spatial dimension

When limiting response peaks over a flat surface, as shown in Figure 1.2, multiple local constraints can be added to limit transfer functions at each point (node) on the surface. However, implementing individual constraints for each point would lead to a very complex TO formulation, as discussed in Section 3.3.2. Similarly, when optimizing for multiple operational frequencies, implementing individual constraints per excitation frequency again leads to a very extensive TO formulation leading to massive computational times. When both problems are combined, i.e., optimizing for multiple excitation frequencies at multiple points, the number of constraints required increase manifold. Thus, there is a need for efficient aggregation of peaks in both dimensions, i.e., spatial and frequency, which can then be employed as constraints in a much more compact manner. Several aggregation functions are available, such as *arithmetic mean, median, mode, range, maximum, minimum* etc. The main objective of an aggregation function is to deliver a single number representing larger data most efficiently and accurately, as per the requirement.

In context with limiting response peaks, there is a need for an aggregation function that delivers a value closest to the maximum absolute peak value of all the response peaks being aggregated. Two aggregation functions are considered in the context of maximum size, *p-mean* and *p-norm*.

3.3.1 p-mean and p-norm

The *p-mean* and *p-norm* functions are defined as follows

$$\begin{aligned} P_m &= \left(\frac{1}{K} \sum_{i=1}^{K} {y_i}^p \right)^{\frac{1}{p}} \\ P_n &= \left(\sum_{i=1}^{K} {y_i}^p \right)^{\frac{1}{p}} \end{aligned} \tag{3.3}$$

where P_m and P_n are *p-mean* and *p-norm* functions respectively. K is the total number of peaks to be aggregated, p is the exponent that controls the accuracy of the aggregation, and y_i is the peak of interest being aggregated.

Both aggregation functions are known to converge to the maximum value of the data set when p approaches infinity [31]. The *p-norm* function is known to overestimate the maximum value while the *p-mean* function underestimates it. Thus, for a given value of p, the maximum value is always bounded from above by the *p-norm* value and below by the *p-mean* value. When limiting peaks, it makes sense to constrain them with an overestimated value, i.e., upper bound to determine the maximum deformation/displacement. So, in this report, *p-norm* function is opted for aggregating peaks.

A significant aspect of using these aggregation functions is that they provide sensitivity information, which is important for gradient-based optimizers. However, it is seen that as the value of p increases, the sensitivities of the smooth aggregation function resemble those of the *max* function [32]. This affects the linearization performed by gradient-based optimizers since sensitivity information seems to be lost for closer approximations of the *max* function. When updating the design variables, the optimizer originally considers a few local constraints. However, a new set of local constraints may stand out as critical or are violated after updating. This leads to oscillations in the optimized design. Hence, the value of p needs to be carefully chosen; a balance must be struck between the accuracy of approximations and sensitivities. The sensitivity of the *p-norm* function is as follows:

$$\begin{aligned}\frac{\partial P_n}{\partial y} &= \frac{\partial\left(\sum {y_i}^p\right)^{\frac{1}{p}}}{\partial y} \\ &= \left(\frac{y_i}{\left(\sum y_i^p\right)^{\frac{1}{p}}}\right)^{p-1} \\ &= \left(\frac{y_i}{P_n}\right)^{p-1}\end{aligned} \tag{3.4}$$

3.3.2 Constraining peaks individually

Consider a model with boundary conditions as shown in Figure 2.2. Input forces are applied at the interface connections modeled as springs. We consider K points on the top surface equidistant to each other, where responses need to be constrained at a single frequency, requiring a total of K constraints. Consider optimization formulation as shown in equation 3.2. Operational frequency ($\omega_j = 3000$Hz) at which response needs to be suppressed is chosen such that it lies between the first and second flexible eigenfrequencies (Ω_4, Ω_5) of the structure (Table 3.1). The maximum response of the structure at top surface at chosen working frequency when no constraints were applied was found to be 0.46 $\mathrm{nm\,N^{-1}}$ (Table 3.1: Case 1, Figure 3.3a). Individual transfer function ($G_k(\omega_j)$) constraints were applied to restrict responses to 0.30 $\mathrm{nm\,N^{-1}}$.

Table 3.2: Results: constraining transfer function individually at some specified points on top surface at ω_j = 3000 Hz

Case	No. of points (K) / constraints	Max. response peak ($G_k(\omega_j)$)	Time / itr. (s)
1	None	0.46 nm N^{-1}	1.31
2	1	0.30 nm N^{-1}	1.90
3	2	0.30 nm N^{-1}	2.35
4	3	0.30 nm N^{-1}	2.87
5	4	0.30 nm N^{-1}	3.46
6	5	0.30 nm N^{-1}	3.69
7	6	0.30 nm N^{-1}	4.29
8	261	0.30 nm N^{-1}	$\approx$ **125**

A summary of results for constraining transfer function individually at some specified points on top surface at prespecified ω_j = 3000 Hz, can be seen in Table 3.2. It can be observed that computational time per iteration increases as the number of constraints are increased. Also, it was observed that it is strenuous for the optimizer to satisfy a large number of constraints together because some constraints are violated at each iteration step, and convergence becomes difficult. It is to be noted that such complications are faced in spite of only a few points considered on the top surface. If the response on all points on the top surface is constrained, i.e., for our considered model, 261 nodes, i.e., 261 constraints, the calculations would be very time taxing for the optimizer owing to many constraints being handled together. It was interpolated through least squares fit (Section 4.1) and approximated that 261 constraints would require about 125 s per iteration. This further reduces the size of the feasible region, and still, a converged result is not guaranteed. So, aggregation of peaks becomes crucial in the spatial dimension. The optimized design for Case 5 i.e. 4 constraints can be seen in Figure 3.4a.

3.3.3 Aggregation of multiple peaks

When aggregating peaks in spatial dimension, for example, all the points (nodes) on a flat surface, we require responses at each considered point ($\mathbf{c}_1, \mathbf{c}_2, ..., \mathbf{c}_k$) (Figure 2.2). The top layer displacements or transfer functions can be aggregated to approximate the maximum response at the top layer of the structure. The constraints can be formulated as a *p-norm* function of transfer functions of nodes at the top surface

$$\begin{aligned} G_{\text{top},\,P_n}(\omega_j) &\leq g_{\text{upp}}(\omega_j) \\ G_{\text{top},\,P_n}(\omega_j) &= \left(\sum_{i=1}^{K} G_i(\omega_j)^p \right)^{\frac{1}{p}} \end{aligned} \tag{3.5}$$

where K is the number of nodes on top surface of the structure. For ease of understanding, we denote $G_{\text{top},\,P_n}(\omega_j)$ as $G_{\text{top, max}}(\omega_j)$.

For lower values of p (2 to 10), constraints were infeasible because of the overestimation of the maximum. This is due to lower accuracy of approximations as when the value of p was increased, the optimizer could restrict response at stricter constraints. Although, when value of p is increased further, the *p-norm* of transfer functions is computed to zero due to smaller values of transfer function (order 1×10^{-9}) being raised to higher exponents (p = 50). This is called numerical underflow,

i.e., values computed are smaller than the smallest number that can be displayed on the computer. This is usually solved by scaling, although at the risk of loss in accuracy of sensitivities at higher values of p. After some inspection, a value of p as 20 was observed suitable for formulations in this work.

Table 3.3: Results: constraining *p-norm* of transfer function at nodes on top surface at ω_j = 3000 Hz

Case	No. of points (K)	Response constraints	Time / itr. (s)
1	4	$G_{1,2,3,4,\max}(\omega_j) \leq 0.3\ \mathrm{nm\,N^{-1}}$	1.85
2	261	$G_{\text{top, max}}(\omega_j) \leq 0.3\ \mathrm{nm\,N^{-1}}$	2.03

(a) Table 3.2, Case 5: individual constraints for 4 nodes

(b) Table 3.3, Case 1: *p-norm* constraint for 4 nodes

(c) Table 3.3, Case 2: *p-norm* constraint for all nodes on top surface

Figure 3.4: Optimized designs for constraining transfer function at some specified points on top surface at ω_j = 3000 Hz

A summary of results for constraining *p-norm* of transfer function at nodes on top surface at pre-specified ω_j = 3000 Hz, can be seen in Table 3.3. It can be seen that there is a huge difference in the computational times as compared to results in Table 3.2. Individually constraining four constraints took almost 3.5 seconds per iteration, while the aggregated constraint of responses at four points takes less than 2 seconds per iteration. The optimized designs (Figure 3.4) for both cases are the same, validating the results.

Next, all displacements on the top surface were aggregated using *p-norm* and constrained. As opposed to 125 s per iteration if all points were constrained individually, the *p-norm* aggregated constraint took just about 2 s per iteration. It was observed and must be noted that for a small number of points, the optimizer could restrict responses to much lower values, albeit at the cost of increased amplitudes at other points on the top surface. However, when all nodes at the top surface are considered, the responses can be restricted only up to certain values. The change in optimized designs (Figure 3.4) from those optimized earlier could be seen as a result of restricting responses at all points on the top surface rather than just four points. This resulted in an increase in the number of branches in the structure connecting to the top surface.

3.4 Aggregation in frequency dimension

Some structures may be subject to external vibrations with their excitation frequency bands lying in the range of eigenfrequencies of the structure. In such cases, responses need to be restricted at all the frequency points in the working frequency excitation bands apart from the eigenfrequencies of the structure. For this, let us first understand how eigenfrequencies are modified during the optimization process when constraining responses at any subject frequency close to the eigenfrequency of the structure.

3.4.1 Constraining frequency peaks individually

Consider a model with boundary conditions as shown in Figure 2.2. Responses at top right node on top surface ($\mathbf{c_{TR}}$) are suppressed at each individual excitation frequency (S_ω = [1700, 1800, 1900, 2000] Hz) lying in the range of higher (flexible) eigenfrequencies of the structure ($\Omega_4, \Omega_5, \Omega_6$) (Table 3.1). The maximum response of the structure at top right node at chosen working frequencies when no constraints were applied was found to be 0.6 $\mathrm{nm\,N^{-1}}$ (Table 3.1: Case 1, Figure 3.3a). Individual transfer function ($G_k(\omega_j)$) constraints are applied to restrict responses to 0.1 $\mathrm{nm\,N^{-1}}$.

Table 3.4: Results: constraining transfer function individually at top right node

Case	Constraints	Ω_4 (Hz)	Ω_5 (Hz)	Ω_6 (Hz)
1	$G_{\mathrm{TR}}(1700\mathrm{Hz}) \leq 0.1\ \mathrm{nm\,N^{-1}}$	1906 ↑	3688	6772
2	$G_{\mathrm{TR}}(1800\mathrm{Hz}) \leq 0.1\ \mathrm{nm\,N^{-1}}$	1927 ↑	3667	6709
3	$G_{\mathrm{TR}}(1900\mathrm{Hz}) \leq 0.1\ \mathrm{nm\,N^{-1}}$	1768 ↓	3763	6616
4	$G_{\mathrm{TR}}(2000\mathrm{Hz}) \leq 0.1\ \mathrm{nm\,N^{-1}}$	1766 ↓	3756	6466

A summary of results for constraining transfer function at TR node at subject frequencies can be seen in Table 3.4. The FRFs of the optimized designs can be seen in Figure 3.5. It can be observed that the fourth eigenfrequency of the structure (Ω_4) is optimized to avoid the excitation frequency at which response is constrained. For cases 1 and 2, Ω_4 increases and obtains a value higher than the excitation frequency, while for the latter two cases, the excitation frequency drops to values lower than the excitation frequency.

The optimized designs can be seen in Figure 3.6. A truss formation characterizes the optimized designs of the first two cases in the right part of the structure. This corresponds with the higher value of Ω_4 to impart more stability for that particular eigenmode. However, this truss starts disappearing for the latter two cases, evidenced by a drop in the value of Ω_4.

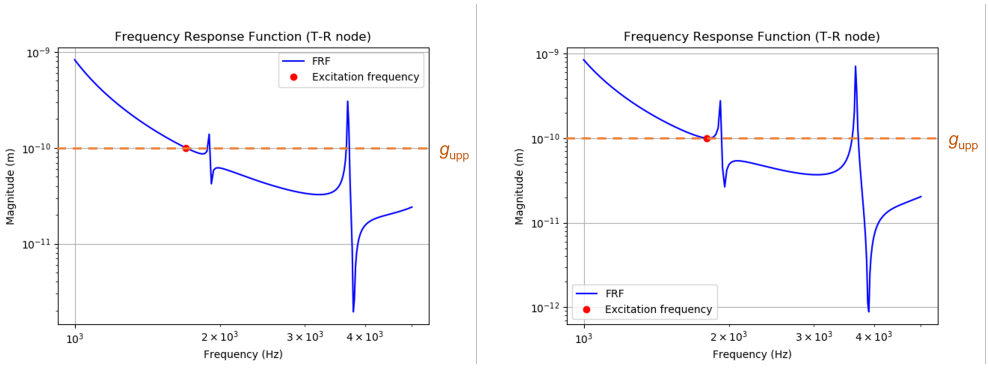

(a) Case 1: ω_j = 1700 Hz

(b) Case 2: ω_j = 1800 Hz

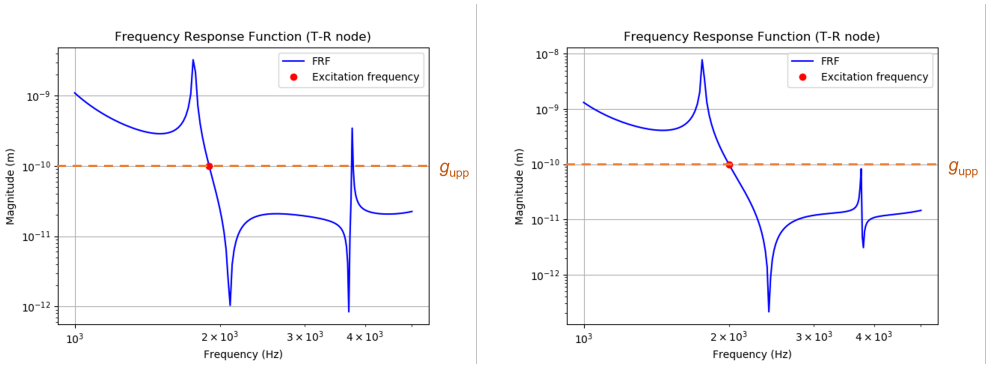

(c) Case 3: ω_j = 1900 Hz

(d) Case 4: ω_j = 2000 Hz

Figure 3.5: FRFs for constraining transfer function at top right node individually (Table 3.4)

(a) Case 1: ω_j = 1700 Hz

(b) Case 2: ω_j = 1800 Hz

(c) Case 3: ω_j = 1900 Hz

(d) Case 4: ω_j = 2000 Hz

Figure 3.6: Optimized designs for constraining transfer function individually at top right node (Table 3.4)

3.4.2 Constraining multiple frequency response peaks

In the previous section, we saw how an eigenfrequency of a structure is modified or optimized subject to constraining responses at excitation frequencies close to that particular eigenfrequency. In this section, we examine the effects on eigenfrequencies and resonant peaks when a structure is to be optimized for constraining responses in a set or band of excitation frequencies.

Consider a model with boundary conditions as shown in Figure 2.2. Responses at top right node on top surface ($\mathbf{c_{TR}}$) need to be suppressed at working excitation frequencies band (S_ω = [1700 : 2000] Hz) lying in the range of higher (flexible) eigenfrequencies of the structure ($\Omega_4, \Omega_5, \Omega_6$) (Table 3.1). The maximum response of the structure at top right node at chosen working frequencies when no constraints were applied was found to be 0.6 $\mathrm{nm\,N^{-1}}$ (Table 3.1: Case 1, Figure 3.3a). Multiple transfer function ($G_k(\omega_j)$) constraints are applied to restrict responses to 0.1 $\mathrm{nm\,N^{-1}}$.

Table 3.5: Results: constraining responses at top right node at frequency band S_ω = [1700:2000] Hz

Case	Constraints	Ω_4 (Hz)	Ω_5 (Hz)	Ω_6 (Hz)	Time / itr. (s)
1	$G_{\mathrm{TR}}(1700\mathrm{Hz}) \leq 0.1\ \mathrm{nm\,N^{-1}}$	1903	3687	6810	4.21
	$G_{\mathrm{TR}}(2000\mathrm{Hz}) \leq 0.1\ \mathrm{nm\,N^{-1}}$	$\Omega_4\ \epsilon\ S_\omega$			
2	$G_{\mathrm{TR}}(1700\mathrm{Hz}) \leq 0.1\ \mathrm{nm\,N^{-1}}$	1926	3682	6783	7.71
	$G_{\mathrm{TR}}(1800\mathrm{Hz}) \leq 0.1\ \mathrm{nm\,N^{-1}}$	$\Omega_4\ \epsilon\ S_\omega$			
	$G_{\mathrm{TR}}(1900\mathrm{Hz}) \leq 0.1\ \mathrm{nm\,N^{-1}}$				
	$G_{\mathrm{TR}}(2000\mathrm{Hz}) \leq 0.1\ \mathrm{nm\,N^{-1}}$				
3	$G_{\mathrm{TR}}(1700\mathrm{Hz}) \leq 0.1\ \mathrm{nm\,N^{-1}}$	No results			
	$G_{\mathrm{TR}}(2000\mathrm{Hz}) \leq 0.1\ \mathrm{nm\,N^{-1}}$				
	$G_{\mathrm{TR}}(\Omega_4) \leq 0.1\ \mathrm{nm\,N^{-1}}$	infeasible			
4	$G_{\mathrm{TR}}(1700\mathrm{Hz}) \leq 0.1\ \mathrm{nm\,N^{-1}}$	1600 ↓	3816	6739	3.91
	$G_{\mathrm{TR}}(2000\mathrm{Hz}) \leq 0.1\ \mathrm{nm\,N^{-1}}$				
	$\Omega_4 \leq 1600\mathrm{Hz}$				
5	$G_{\mathrm{TR}}(1700\mathrm{Hz}) \leq 0.1\ \mathrm{nm\,N^{-1}}$	2268 ↑	4168	5713	2.82
	$G_{\mathrm{TR}}(2000\mathrm{Hz}) \leq 0.1\ \mathrm{nm\,N^{-1}}$				
	$\Omega_4 \geq 2000\mathrm{Hz}$				

A summary of results for constraining responses at top right node at prespecified frequency band S_ω = [1700:2000] Hz can be seen in Table 3.5. The FRFs of the optimized designs can be seen in Figure 3.7. The first case involves directly constraining peaks at the lower and upper limits of the frequency band. As can be seen, the value of Ω_4 lies inside the frequency band (S_ω), which is not desired since it will lead to high deformations when excitation frequency (ω_j) is equal to the eigenfrequency (Ω_4). We study three alternatives and their efficiency to ensure that the responses are constrained within the frequency band.

1. Inclusion of more frequency points in the given frequency band and constraining peaks at each of these frequencies (Case 2)
2. Constraining resonant peak at eigenfrequency lying in the frequency band (Case 3)

3. Constraining eigenfrequency to restrict its values from lying in the frequency band (Case 4 and Case 5)

Including more frequency points in the specified frequency band did help constrain responses at each of these frequencies but was not enough to push Ω_4 outside S_ω. Also, since more frequency points meant more solutions to a linear system of equations, the computational times were huge. Depending on the number of frequency points, the computational time per iteration elevates quickly.

Constraining the resonant peak at Ω_4 did not produce any results as the resonant peak constraint was infeasible. The magnitude of the transfer function at eigenfrequencies largely depends on the type of damping model being used. The maximum response of the benchmark structure (Table 3.1: Case 1, Figure 3.3a) was observed to be 10 $\mathrm{nm\,N^{-1}}$ which is 2 orders higher than the magnitude we are constraining for. We will examine more on optimizing resonant peaks in the next Chapter (4), but for this case, it makes sense to look at the next proposed alternative.

Constraining eigenfrequency to restrict its values from lying in the frequency band proved fruitful as the optimizer could efficiently limit responses within the frequency band while keeping the subject eigenfrequency (Ω_4) away from the frequency band. It can be observed that implementing eigenfrequency constraints for higher values (Case 5) proved more time efficient since it supported the objective function of maximizing eigenfrequencies.

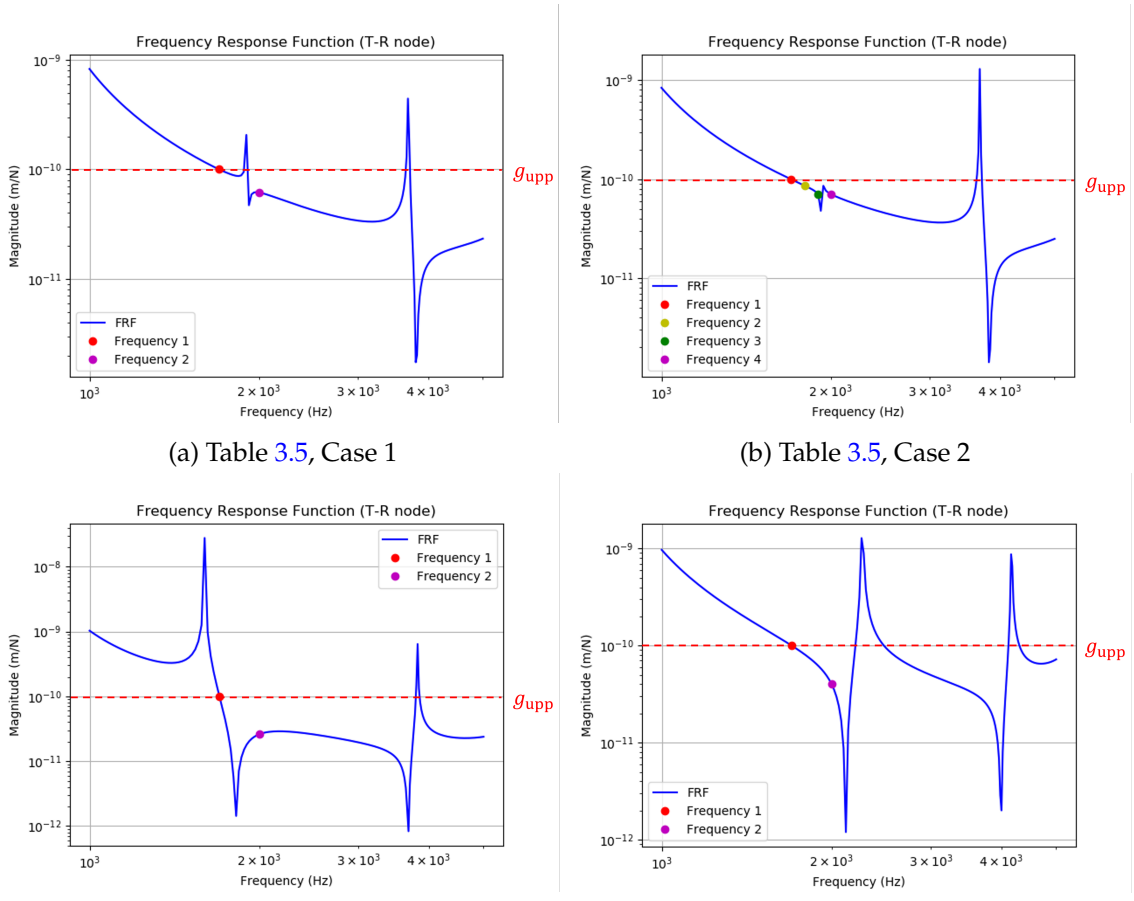

(a) Table 3.5, Case 1

(b) Table 3.5, Case 2

(c) Table 3.5, Case 4

(d) Table 3.5, Case 5

Figure 3.7: FRFs for constraining responses at top right node at frequency band S_ω = [1700:2000] Hz

The final optimized designs can be seen in Figure 3.8. The output designs of Case 1 and Case 2 were observed to be quite similar. Cases 4 and 5 resulted in absolute 1-0 designs. The disappearance of truss formations in the right part of the structure in Case 4 can be attributed to the resulting lower value of Ω_4. Whereas the formation of extra trusses in Case 5 can be attributed to the higher value of Ω_4, providing more stiffness for that particular eigenmode.

(a) Table 3.5, Case 1

(b) Table 3.5, Case 2

(c) Table 3.5, Case 4

(d) Table 3.5, Case 5

Figure 3.8: Optimized designs for constraining responses at top right node at frequency band S_ω = [1700:2000] Hz

3.4.3 Constraining multiple peaks in spatial and frequency domain

Real-life machinery is susceptible to vibrations in a wide range of frequencies. Implementing individual constraints per excitation frequency per node leads to a very extensive TO formulation with massive computational times. Also, it works against the optimizer trying to handle a large number of constraints. This section looks at aggregating peaks in both spatial and frequency dimensions.

Aggregating peaks in spatial domain using *p-norm* function proved fruitful with low computational times. However, aggregation of peaks in the frequency domain is highly inefficient because of eigenfrequencies' inflexibility to optimize. Problems with convergence are faced where a new set of constraints are violated at each iteration when eigenfrequencies approach the subject frequencies. Instead, we look for more imaginative ways to aggregate frequencies. After analyzing the excitation frequency band and the eigenfrequencies of the structure lying in that band, it seems a smart way to restrict eigenfrequencies from lying in the operating frequency bands by applying eigenfrequency constraints, and frequencies can be smartly chosen from the working frequency band to restrict responses for the entire band. The primary purpose would be to make the excitation frequency band (S_ω) lie between two consecutive eigenfrequencies so that responses between the two eigenfrequencies can be efficiently restricted.

Consider a model with boundary conditions as shown in Figure 2.2. Responses at all nodes on top surface ($\mathbf{c}_1, \mathbf{c}_2, ..., \mathbf{c}_k$) need to be suppressed at working excitation frequencies band (S_ω = [3500 : 4500] Hz) lying in the range of higher (flexible) eigenfrequencies of the structure ($\Omega_4, \Omega_5, \Omega_6$) (Table 3.1). The maximum response of the structure at top surface at chosen working frequencies when no

constraints were applied was found to be 0.4 $\mathrm{nm\,N^{-1}}$ (Table 3.1: Case 1, Figure 3.3a). Constraints are applied to restrict responses to 0.3 $\mathrm{nm\,N^{-1}}$.

Table 3.6: Results: constraining responses at all nodes on top surface at frequency band S_ω = [3500 : 4500] Hz

Case	**Constraints**	Ω_4 (Hz)	Ω_5 (Hz)	Ω_6 (Hz)	**Time / itr. (s)**
1	$G_{\text{top, max}}(3500\text{Hz}) \leq 0.3\ \mathrm{nm\,N^{-1}}$	2034	3659	6023	2.85
	$G_{\text{top,max}}(4500\text{Hz}) \leq 0.3\ \mathrm{nm\,N^{-1}}$	$\Omega_5\ \epsilon\ S_\omega$			
2	$G_{\text{top, max}}(3500\text{Hz}) \leq 0.3\ \mathrm{nm\,N^{-1}}$	2097	3300 $\downarrow$	5539	2.67
	$G_{\text{top, max}}(4500\text{Hz}) \leq 0.3\ \mathrm{nm\,N^{-1}}$				
	$\Omega_5 \leq 3300$ Hz				
3	$G_{\text{top, max}}(3500\text{Hz}) \leq 0.3\ \mathrm{nm\,N^{-1}}$	2400	4700 $\uparrow$	5510	2.64
	$G_{\text{top, max}}(4500\text{Hz}) \leq 0.3\ \mathrm{nm\,N^{-1}}$				
	$\Omega_5 \geq 4700$ Hz				

Some formulations are summarized in Table 3.6. As can be clearly seen from FRF graphs shown in Figure 3.9, eigenfrequency constraints are effective in avoiding eigenfrequencies from lying in the excitation frequency band. The responses for frequencies in the frequency band can then be efficiently constrained. The final optimized designs can be seen in Figure 3.10. The disappearance of trusses in Case 2 and the appearance of trusses in Case 3 in the left and right parts of the structure can be largely attributed to obtained values of Ω_5.

Some problems may involve wide frequency ranges of excitations, making it difficult for eigenfrequencies to be pushed out. For such cases, we look for optimizing responses at the eigenfrequencies of the structure. This is explored further in Chapter 4.

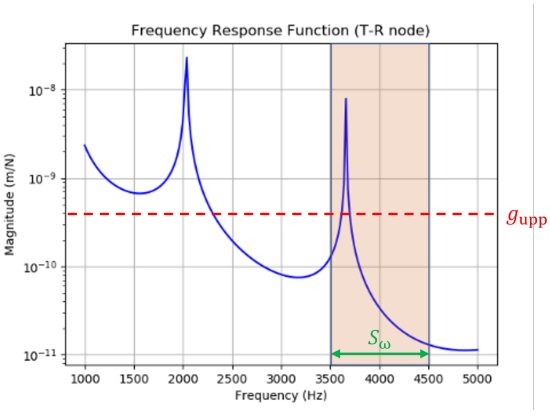

(a) Table 3.6, Case 1

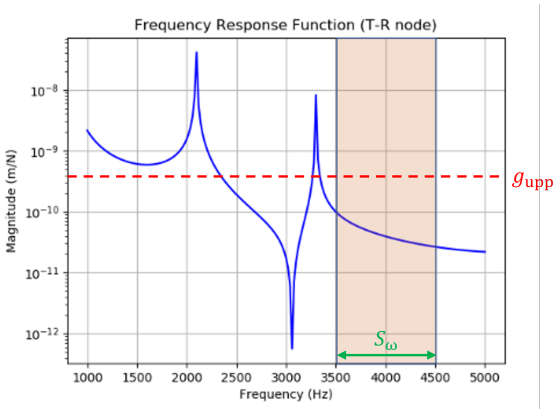

(b) Table 3.6, Case 2

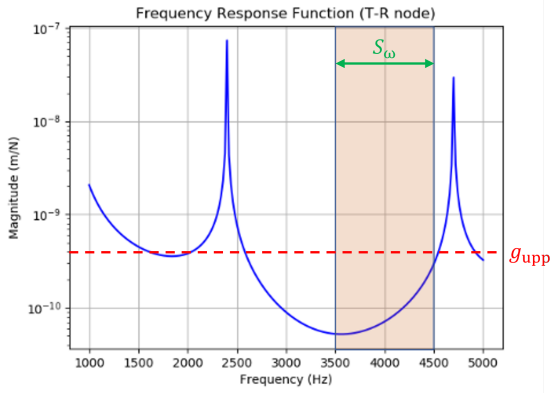

(c) Table 3.6, Case 3

Figure 3.9: FRFs for constraining responses at all nodes at top surface at frequency band S_ω = [3500 : 4500] Hz

(a) Table 3.6, Case 1

(b) Table 3.6, Case 2

(c) Table 3.6, Case 3

Figure 3.10: Optimized designs for constraining responses at all nodes at top surface at frequency band S_ω = [3500 : 4500] Hz

3.5 Interface connections stiffnesses

The interface connection stiffnesses play a pivotal role in deciding the eigenfrequencies of suspension modes of a structure. Refer to our discussions in Section 3.2, where the eigenfrequencies of suspension modes depend mainly on the mass of the structure and the stiffness of the interface connections, while the eigenfrequencies of flexible modes depend on the mass and stiffness of the structure. TO works as a stiffness modulator, where the density of each element is optimized to get the required stiffnesses at each discrete element. When optimizing the eigenfrequencies of suspension modes, the optimizer can only control or modify the mass component of the structure to influence the eigenfrequency. For the stiffness to be modified, it becomes essential to provide interface connection stiffnesses as variables to the optimizer.

Consider the model shown in Figure 2.2a, where eigenfrequencies of the structure need to be maximized. The coefficients of the stiffnesses of the interface connections are provided as variables, while the order of the magnitude has been kept constant. Other formulations for stiffness variables can be implemented per requirements, but we choose a more straightforward formulation for understanding principles. The goal of the optimization (Case 2 and Case 3) is to maximize the eigenfrequencies of the structure by providing both density and interface connection stiffnesses as variables. In another formulation (Case 4), we try to constrain eigenfrequencies $(\Omega_1, \Omega_2, \Omega_3)$ with upper limits and see the effect on optimized stiffnesses of interface connections.

$$\begin{aligned} \min_{\text{a,b,c,d,s}} \quad & \left(\sum_{i=1}^{n} \frac{1}{\Omega_i(\mathbf{s})} \right) \\ \text{s.t.} \quad & V_f \geq 0.5 \\ & s_{\min} \leq \mathbf{s} \leq 1 \end{aligned} \tag{3.6}$$

$$\begin{aligned} k_{1,x} &= a(1 \times 10^7)\ \mathrm{N\,m^{-1}} \\ k_{1,y} &= b(1 \times 10^9)\ \mathrm{N\,m^{-1}} \\ k_{2,x} &= c(1 \times 10^9)\ \mathrm{N\,m^{-1}} \\ k_{2,y} &= d(1 \times 10^9)\ \mathrm{N\,m^{-1}} \\ 0 &\leq a \leq 1 \\ 0 &\leq b \leq 1 \\ 0 &\leq c \leq 1 \\ 0 &\leq d \leq 1 \end{aligned} \tag{3.7}$$

$$\Omega_j^2 - \beta_1 \leq 0, \quad j = 1, 2, 3 \tag{3.8}$$

Table 3.7: Results: Interface connections stiffnesses as variables

Case	Variables	$k_{1,x}$ ($\mathrm{N\,m^{-1}}$)	$k_{1,y}$ ($\mathrm{N\,m^{-1}}$)	$k_{2,x}$ ($\mathrm{N\,m^{-1}}$)	$k_{2,y}$ ($\mathrm{N\,m^{-1}}$)	Ω_1 (Hz)	Ω_2 (Hz)	Ω_3 (Hz)
1	$\mathbf{s}$	1.74e+6	2.70e+8	6.40e+8	2.70e+8	383	646	795
2	$\mathbf{s}$, $k_{1,x}, k_{1,y}$	9.99e+6	9.99e+8	6.40e+8	2.70e+8	403	694	1206
3	$\mathbf{s}$, $k_{1,x}, k_{1,y}, k_{2,x}, k_{2,y}$	9.99e+6	9.99e+8	9.99e+8	9.99e+8	639	893	1402
4	$\mathbf{s}$, $k_{1,x}, k_{1,y}, k_{2,x}, k_{2,y}$	7.81e+6	3.07e+8	4.81e+8	6.97e+8	400	600	800

Table 3.7 gives a summary of results for formulations discussed. In Case 1, we optimize density for maximum eigenfrequencies ($\Omega_1, \Omega_2, \Omega_3$) with spring stiffnesses constant. When spring 1 stiffnesses ($k_{1,x}, k_{1,y}$) are provided as variables (Case 2), we observe an increase in the eigenfrequencies of suspension modes with the spring 1 stiffnesses achieving maximum values. When both spring 1 and spring 2 stiffnesses ($k_{1,x}, k_{1,y}, k_{2,x}, k_{2,y}$) are provided as variables (Case 3), we see a further increase in the eigenfrequencies with all four stiffnesses achieving maximum values. In Case 4, we limit the values of eigenfrequencies of suspension modes with upper limits. We observe that the stiffnesses obtain some specific values instead of maxing out. Figure 3.11 shows the optimized designs for the four formulations.

(a) Case 1

(b) Case 2

(c) Case 3

(d) Case 4

Figure 3.11: Optimized designs for interface connections stiffnesses as variables (Table 3.7)

We have already discussed how the eigenfrequencies of a structure are changed when optimizing response at a particular frequency. With the spring stiffnesses offered as variables to the optimizer, it is possible to optimize response for frequencies lying in the range of low eigenfrequencies, i.e., suspension modes, since, along with mass, stiffnesses can also be optimized to influence the subject eigenfrequencies. One may question that the spring stiffnesses would be maxed out during the optimization process for eigenfrequency maximization. We saw in Section 3.4.1 how a particular eigenfrequency obtained a lower value than the subject working frequency when constraining responses. Providing interface connections stiffnesses as variables and optimizing responses at some frequencies could very well lead to designing high pass and low pass filters where vibrations below or above a specified cut-off frequency are attenuated.

3.6 Conclusion

This Chapter aimed to investigate and develop TO methods to suppress vibrations on a flat surface for suspended structures. Based on discussions in this Chapter, some conclusions can be drawn out and summarized as follows:

1. For non-collocated I/O systems, transfer functions should be considered as constraints to impart meaning to TO formulation. Mean-eigenvalue is implemented as the objective function.
2. Influence of suspension and flexible modes on the objective function is inspected. Suspension modes must be included to ensure structure formation relevant to boundary conditions, while flexible modes can be chosen based on the highest frequency bands of excitations.
3. It was observed that the inclusion of suspension modes in the objective function compels the optimizer to push towards lower volume structures. Thus, weight minimization is implicitly achieved in the mean eigenvalue objective function, and volume constraints can be incorporated into the formulation as per requirements.
4. To optimize response at frequencies lying in the range of eigenfrequencies of suspension modes, stiffnesses of interface connections must be provided as variables to the optimizer along with the density variable. This is because eigenfrequencies of suspension modes depend on the mass of the structure and the stiffness of interface connections.
5. Aggregating response peaks at a single frequency in spatial domain using *p-norm* function proved very effective and efficient. Aggregation reduced computational times by 47% for four peaks and approximated 98% for 261 peaks as per our model.
6. Aggregation of peaks in the frequency domain using *p-norm* function was proved infeasible. Frequency is fundamentally different from space which makes it difficult for aggregation. When frequency response peaks are aggregated using *p-norm* function, the optimizer compels eigenfrequencies lying in the frequency band to approach the subject frequencies, which are marked with convergence issues. Though, aggregating resonant peaks using *p-norm* function is quite feasible (Appendix D), where convergence issues are avoided.
7. To restrict frequency responses, it is efficient and effective to apply transfer function constraints at lower and upper limits of the frequency band and eigenfrequency constraints to avoid them from lying in the frequency band. Problems involving wide frequency ranges of excitation make it difficult for the eigenfrequencies to be optimized and pushed out of the operating frequency bands. For such problems, we look for optimizing response at the subject eigenfrequencies, which is explored further in Chapter 4.

Chapter 4

Dynamic Global Flatness

In Chapter 3, we investigated how to limit or constrain vibration levels at some or all points (nodes) on a flat surface for a non-collocated I/O system. However, apart from limiting responses, some applications require the surfaces to remain flat for precise functioning. One such example can be seen in the form of MEMS (Microelectromechanical systems) deformable mirror, where adaptive optics are used to correct for various aberrations induced by the environment and imperfections in fixed optics used in these instruments [23]. For such applications, relative displacements between nodes are more critical than their individual displacements. In this Chapter, we study surface flatness and its measures and later incorporate it into our TO framework.

Surface flatness is defined as the deviation in the height of the surface relative to a reference plane over short distances in a local area [21]. When this measure is considered over a larger scale, such as the entire surface (of a platform or a stage), it is termed global flatness, as illustrated in Figure 1.3. Local flatness is assessed to find minor gaps or imperfections on the slab, whereas global flatness is controlled to discover more significant deformations, like bending. Global flatness is defined for static systems, mainly from a manufacturing point of view. While, for dynamical, i.e., moving systems, it has been mostly associated with control systems where sensors and actuators are employed for flatness measurement, and correction [22].

When talking about global flatness, modifying mode shapes comes into the picture automatically. A strategy was proposed for synthesizing desired eigenfrequencies, and eigenmode amplitudes at certain points of the structure [33]. A method was developed to modify existing mode shapes to desired ones using modal assurance criterion [34]. An approach was also presented for tailoring user-defined vibration modes to design functionally graded piezoelectric transducers [35]. However, it was observed that only certain parts of an eigenmode shape could be user-defined or prespecified. Therefore, tailoring mode shapes are practical when designing actuators where response needs to be maximized at specific points on the structure, i.e., some part of the eigenmode shape is maximized according to its desired dynamic response, as opposed to other regions which remain unspecified because of their undesirable dynamic response. Thus, this method results in increased response at some points on the structure at the cost of reducing responses at other points. This might be effective for local flatness problems, but as per our needs, suppression of relative vibration amplitudes globally at all points on the top surface is highly unlikely through this approach.

For a dynamically moving surface to remain flat, ideally, the nodal displacements of the surface should remain in the same phase, i.e., their phase must be synchronized. Apart from their phase synchronization, the flatness of the surface must be ensured with a flatness fit. Thus, we look for measures that can directly influence the relative displacements of each point on the top surface of the structure. One such method is the Least Squares Method [36], which is discussed in detail in Section 4.1.

Consider our model from previous chapter (Figure 2.2). When excited at its 4^{th} eigenfrequency, the structure undergoes deformation as shown in Figure 4.1a. The displacements of top surface nodes are in the form of complex values ($\mathbf{u}(\omega)$). When restricting responses at some or all points on a flat surface, the magnitude of $\mathbf{u}(\omega)$ is used to obtain the amplitude of displacements. However, using the magnitude of $\mathbf{u}(\omega)$ for least squares fit (LSF) to incorporate dynamic flatness poses complexities. Figure 4.1b shows the magnitude of displacements $|\mathbf{u}(\omega)|$ of top layer nodes when the structure is excited at operational frequency, ω_p equal to Ω_4, which is the first flexible eigenmode. The nodal displacements (from b to c) which are out of phase with other nodal displacements (from a to b and c to d) become absolute when the magnitude of $\mathbf{u}(\omega)$ is considered. Thus, employing an LSF on magnitudes of displacement is meaningless as important phase information is lost when absolute values are considered.

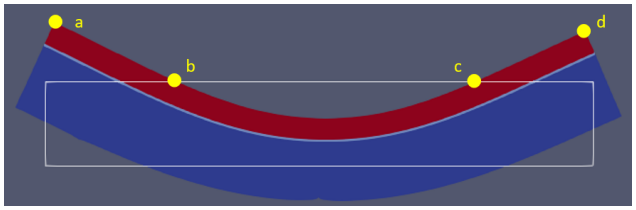

(a) Deformation of model structure at $\omega_p = \Omega_4$

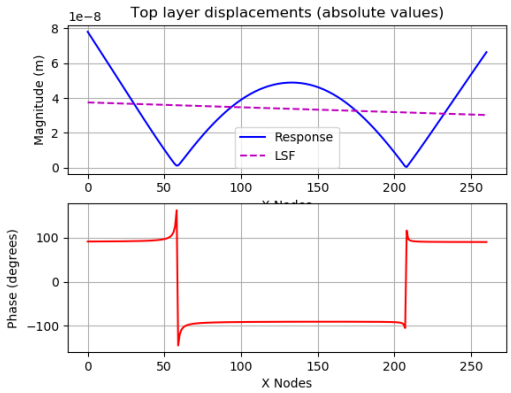

(b) Magnitude and phase of $\mathbf{u}_{\text{top}}(\Omega_4)$

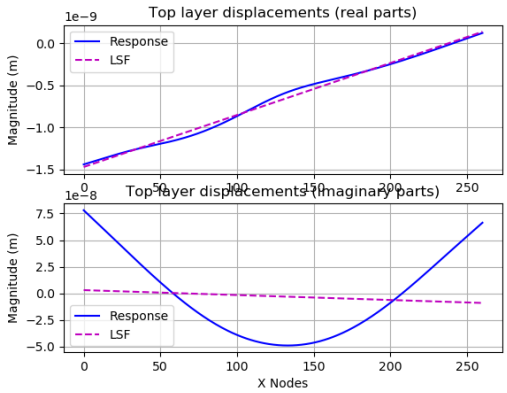

(c) Real and imaginary components of $\mathbf{u}_{\text{top}}(\Omega_4)$

Figure 4.1: Problem faced with employing LSF on magnitude of displacement $|\mathbf{u}_{\text{top}}(\Omega_4)|$

Therefore, to ensure the global dynamical flatness of a surface, the phase difference of each node is crucial to the problem. Apart from employing a flatness fit, i.e., LSF on the nodal displacements, one must also ensure that all nodal displacements are synchronized in phase. We begin by understanding the least squares method, its sensitivities, and how it is essential to our problem for flatness fit.

4.1 Least Squares Method

The least squares method is probably one of the most popular and oldest techniques in statistics. The least squares express the variance in the dependent variable as a function of the independent variable. Refer to Figure 4.2, where displacements of a surface are plotted along the domain of the surface. The least squares method minimizes the sum of squared deviations, i.e., residuals, to obtain the least squares fit. The least squares method further quantifies the deviations in the observed values from the fitted curve. Relative to our problem, we look to minimize (constrain) the sum of squared deviations in displacements of top surface nodes to employ a flatness fit.

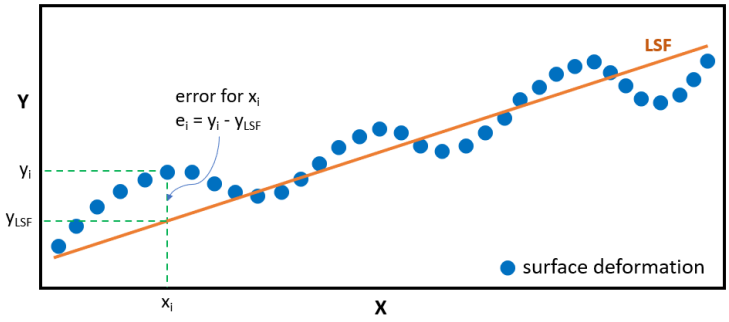

Figure 4.2: Surface flatness: the measure of deviations in the height of the surface through least squares method

Let us assume our least square fit linear model in matrix form is given by

$$\mathbf{y} = \mathbf{X}\mathbf{b} + \mathbf{e} \tag{4.1}$$

where

$$\mathbf{y} = \begin{pmatrix} y_1 \\ . \\ . \\ . \\ y_n \end{pmatrix}, \quad \mathbf{X} = \begin{pmatrix} 1 & x_{21} & \dots & x_{k1} \\ . & . & \dots & . \\ . & . & \dots & . \\ . & . & \dots & . \\ 1 & x_{2n} & \dots & x_{kn} \end{pmatrix}, \quad \mathbf{b} = \begin{pmatrix} b_1 \\ . \\ . \\ . \\ b_k \end{pmatrix}, \quad \mathbf{e} = \begin{pmatrix} e_1 \\ . \\ . \\ . \\ e_n \end{pmatrix} \tag{4.2}$$

In the n x k matrix $\mathbf{X} = (x_{ji})$, the first index $j (j = 1, ..., k)$ refers to the variable number (in columns) and the second index $i (i = 1, ..., n)$ refers to the observation number (in rows). Here $\mathbf{b}$ is a k x 1 vector of unknown parameters, and $\mathbf{e}$ is an n x 1 vector of unobserved disturbances, i.e., residuals, which can be computed by the means of

$$\mathbf{e} = \mathbf{y} - \mathbf{X}\mathbf{b} \tag{4.3}$$

To determine the least squares estimator, we write the sum of squares of the residuals (a function of $\mathbf{b}$) as

$$\begin{aligned} S(\mathbf{y}, \mathbf{b}) = \sum \mathbf{e_i^2} = \mathbf{e}^{\mathrm{T}}\mathbf{e} = (\mathbf{y} - \mathbf{X}\mathbf{b})^{\mathrm{T}}(\mathbf{y} - \mathbf{X}\mathbf{b}) \\ = \mathbf{y}^{\mathrm{T}}\mathbf{y} - \mathbf{y}^{\mathrm{T}}\mathbf{X}\mathbf{b} - \mathbf{b}^{\mathrm{T}}\mathbf{X}^{\mathrm{T}}\mathbf{y} + \mathbf{b}^{\mathrm{T}}\mathbf{X}^{\mathrm{T}}\mathbf{X}\mathbf{b} \end{aligned} \tag{4.4}$$

The least squares estimator is obtained by minimizing $S(\mathbf{b})$. Therefore, we set $\frac{\partial S}{\partial \mathbf{b}}$ equal to zero

$$\frac{\partial S}{\partial \mathbf{b}} = -\mathbf{2}\mathbf{X}^{\mathrm{T}}\mathbf{y} + \mathbf{2}\mathbf{X}^{\mathrm{T}}\mathbf{X}\mathbf{b} = 0 \tag{4.5}$$

which gives us

$$\mathbf{X}^{\mathrm{T}}\mathbf{X}\mathbf{b} = \mathbf{X}^{\mathrm{T}}\mathbf{y} \tag{4.6}$$

Solving this for $\mathbf{b}$, we get

$$\mathbf{b} = (\mathbf{X}^{\mathrm{T}}\mathbf{X})^{-\mathbf{1}}\mathbf{X}^{\mathrm{T}}\mathbf{y} \tag{4.7}$$

provided that the inverse of $\mathbf{X}^{\mathrm{T}}\mathbf{X}$ exists, which means matrix $\mathbf{X}$ should have rank k. For the formulations in this work, we employ a linear least square fit, i.e., the value of k is 2.

For the computation of design sensitivities, we need to determine how the sum of squares of the residuals $S(\mathbf{b})$ varies with the displacements $\mathbf{y}$.

$$\frac{\partial S}{\partial \mathbf{y}} = 2\mathbf{e}\frac{\partial \mathbf{e}}{\partial \mathbf{y}} = 2\Big(\mathbf{y} - \mathbf{X}\mathbf{b}\Big)\Big(1 - \mathbf{X}\frac{\partial \mathbf{b}}{\partial \mathbf{y}}\Big) \tag{4.8}$$

where

$$\frac{\partial \mathbf{b}}{\partial \mathbf{y}} = (\mathbf{X}^{\mathrm{T}}\mathbf{X})^{-\mathbf{1}}\mathbf{X}^{\mathrm{T}} \tag{4.9}$$

Therefore,

$$\begin{aligned}
\frac{\partial S}{\partial \mathbf{y}} &= 2\Big(\mathbf{y} - \mathbf{X}\mathbf{b}\Big)\Big(1 - \mathbf{X}(\mathbf{X}^{\mathrm{T}}\mathbf{X})^{-\mathbf{1}}\mathbf{X}^{\mathrm{T}}\Big) \\
&= 2\Big(\mathbf{y} - \mathbf{X}\mathbf{b}\Big)\Big(1 - \mathbf{X}\frac{\mathbf{b}}{\mathbf{y}}\Big) \\
&= \frac{2}{\mathbf{y}}(\mathbf{y} - \mathbf{X}\mathbf{b})^2 \\
&= \frac{2}{\mathbf{y}}\mathbf{e}^{\mathrm{T}}\mathbf{e}
\end{aligned} \tag{4.10}$$

4.2 Problem formulation

As per our discussions in the introduction, to ensure the global dynamical flatness of a surface, there are two challenges we face:

1. Top surface nodal displacements should remain in the same phase, i.e., their phase must be synchronized.
2. LSF can not be applied to the magnitude of displacements of the top surface since crucial phase information is lost when absolute values are considered.

The displacement of a particular node k can be expressed in complex form as shown:

$$\mathbf{u}_k(\omega, t) = \Re(\mathbf{u}_k) + \Im(\mathbf{u}_k) \tag{4.11}$$

The magnitude and phase of the displacement of node k are as follows:

$$\begin{aligned}
|\mathbf{u}_k(\omega)| &= \sqrt{\Re(\mathbf{u}_k)^2 + \Im(\mathbf{u}_k)^2} \\
\boldsymbol{\phi}_k &= \tan^{-1}\left(\frac{\Im(\mathbf{u}_k)}{\Re(\mathbf{u}_k)}\right)
\end{aligned} \tag{4.12}$$

Having a closer look at the real and imaginary components of the top surface displacements, when the structure is excited at its 4^{th} eigenfrequency ($\mathbf{u}(\Omega_4)$), the imaginary parts (order 1×10^{-8}) are more significant than the real parts (order 1×10^{-9}) which result in huge phase differences as can be seen in Figure 4.1c. For phase synchronization, it is essential to constrain the imaginary parts, so their values are comparatively lower than the real ones. This will ensure that the maximum phase difference between top surface nodal displacements is within the specified limit.

Phase constraint (g_{phase}):

$$\frac{P_n\big(\Im(\mathbf{u}_{\text{top}}(\omega))\big)}{P_n\big(\Re(\mathbf{u}_{\text{top}}(\omega))\big)} \leq \gamma \tag{4.13}$$

where P_n is the *p-norm* function used to compute the smooth maximum of real and imaginary parts of displacement. By restricting the phase difference, we ensure that all points on the top surface move together in the same phase (ideally). Additionally, for the surface to maintain its flatness, we employ LSF to constrain the shape of amplitudes of displacement. By application of phase constraint, the imaginary component values are reduced to achieve lower phase differences. Therefore, the real components (now more significant than imaginary components) determine the amplitude of displacement and shape of structure when excited harmonically. Therefore, we implement the LSF on the displacement's real components to constrain the structural response's shape.

LSF constraint (g_{fit}):

$$S\big(\Re(\mathbf{u}_{\text{top}}(\omega))\big) \leq \alpha \tag{4.14}$$

Let us consider our benchmark design (Table 3.1: Case 1, Figure 3.3a). The response (top layer displacements) of the structure at $\omega_p = 3000\text{Hz}$ is shown in Figure 4.3. The response of the structure at $\omega_p = \Omega_4$ is shown in Figure 4.4.

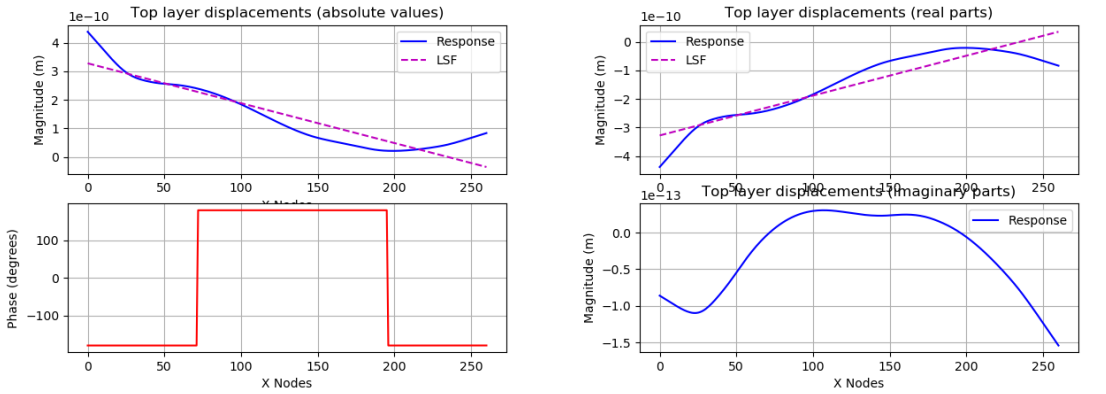

(a) Magnitude and phase of $\mathbf{u}_{\text{top}}$

(b) Real and imaginary components of $\mathbf{u}_{\text{top}}$

Figure 4.3: Top layer displacements of benchmark design at $\omega_p = 3000\text{Hz}$

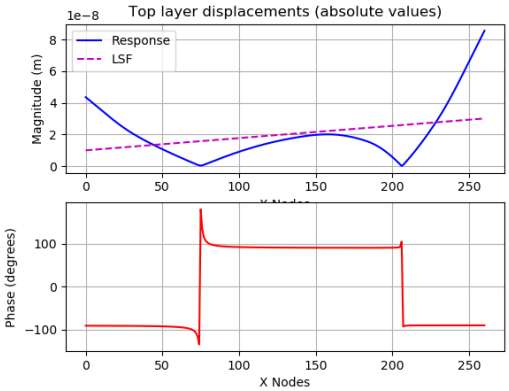

(a) Magnitude and phase of $\mathbf{u}_{\text{top}}$

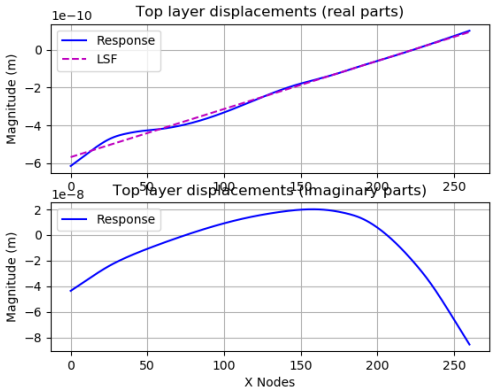

(b) Real and imaginary components of $\mathbf{u}_{\text{top}}$

Figure 4.4: Top layer displacements of benchmark design at $\omega_p = \Omega_4$

When the structure is excited at $\omega_p = 3000\text{Hz}$, the imaginary components (order 1×10^{-13}) are much lower as compared to the real components (order 1×10^{-10}) which result in desirable phase differences (either 180° or -180°) as far as dynamic flatness is considered. While, when the structure is excited at its 4^{th} eigenfrequency ($\omega_p = \Omega_4$), the imaginary parts (order 1×10^{-8}) are greater than the real parts (order 1×10^{-10}) which result in huge undesirable phase differences. Therefore, for achieving dynamic flatness at operating frequencies other than eigenfrequencies, only the shape of the real parts needs to be constrained. While, for operating frequencies ($\omega_p = \Omega$), both shape and phase need to be constrained to achieve dynamic flatness.

Based on these considerations, a TO problem for achieving dynamic global flatness at a particular working frequency (ω) can be formulated as follows:

$$\begin{aligned} \min_{\mathbf{s}} \quad & \left(\sum_{i=1}^{n} \frac{1}{\Omega_i(\mathbf{s})} \right) \\ \text{s.t.} \quad & \frac{P_n\big(\Im(\mathbf{u}_{\text{top}}(\omega))\big)}{P_n\big(\Re(\mathbf{u}_{\text{top}}(\omega))\big)} \leq \gamma \\ & S_{\Re(\mathbf{u}_{\text{top}}(\omega))} \leq \alpha \\ & V_f \geq 0.5 \\ & s_{\min} \leq \mathbf{s} \leq 1 \end{aligned} \tag{4.15}$$

For simplicity, we further abbreviate the phase constraint shown in Equation 4.13 as g_{phase} and LSF constraint shown in Equation 4.14 as g_{fit}. For formulations in this work, value of γ was chosen as 0.10 to keep imaginary components $\frac{1}{10}^{\text{th}}$ of the real components. Value of α was chosen as 1×10^{-10}.

4.3 Results

We apply the TO formulation as given in Equation 4.15 to achieve dynamic global flatness at 4^{th} eigenfrequency (Ω_4) of the structure. The objective function value is scaled to 100 for the first iteration. The constraints are scaled such that their first iteration values lie from 1 to 10. The termination condition for all optimizations was convergence at design variable tolerance of 1×10^{-4}. The convergence plot for the dynamic flatness constraints, i.e., the LSF constraint and phase constraint, can be seen in Figure 4.5.

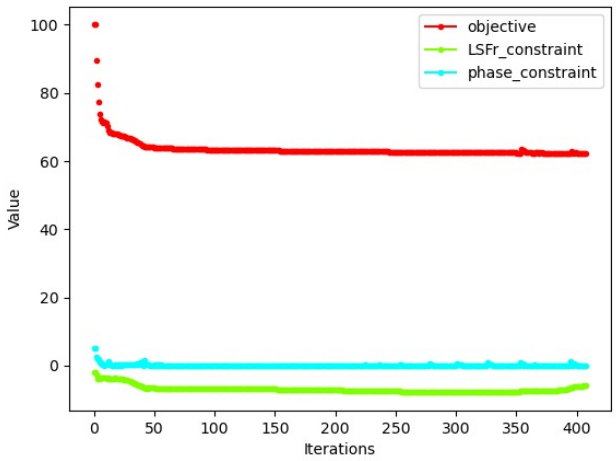

Figure 4.5: Convergence plot: dynamic flatness constraints

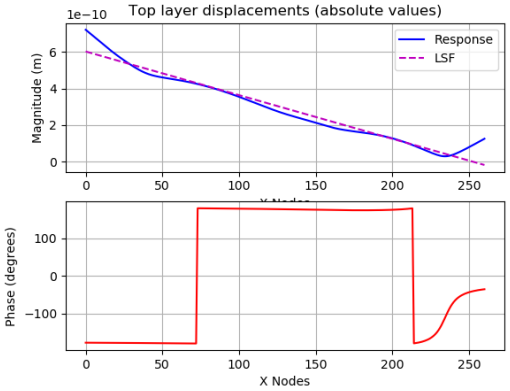

(a) Magnitude and phase of $\mathbf{u}_{\text{top}}$

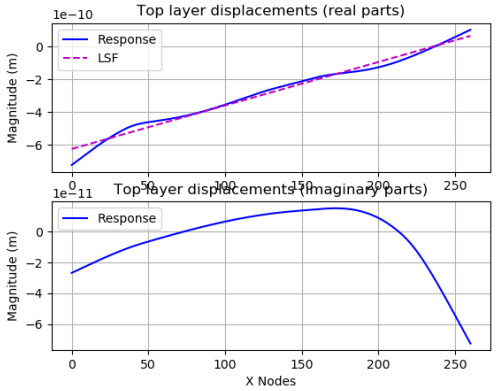

(b) Real and imaginary components of $\mathbf{u}_{\text{top}}$

Figure 4.6: Top layer displacements of optimized design at $\omega_p = \Omega_4$

The top layer displacements: absolute, real, and imaginary components of the optimized design can be seen in Figure 4.6. The effect of the constraints was as desired, the top layer displacements (absolute values) were found to be in accordance with a flat surface. The phase constraint made sure that all the points on the top surface were moving together (phase $180°$ or $-180°$). The LSF constraint constrained the shape of the top surface to ascertain its flatness. The kink in absolute values in Figure 4.6a could be seen as a result of negative values becoming absolute when the magnitude is considered.

(a) Benchmark design without constraints

(b) Optimized design with dynamic flatness constraints

Figure 4.7: Comparison of benchmark and optimized designs

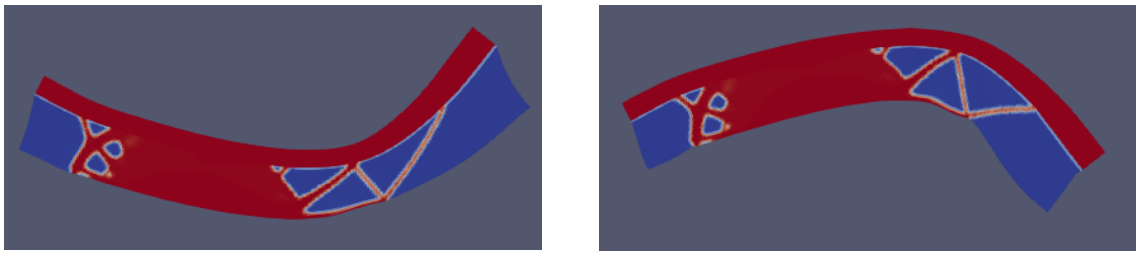

Figure 4.8: Benchmark design: motion when excited at $\omega_p = \Omega_4$

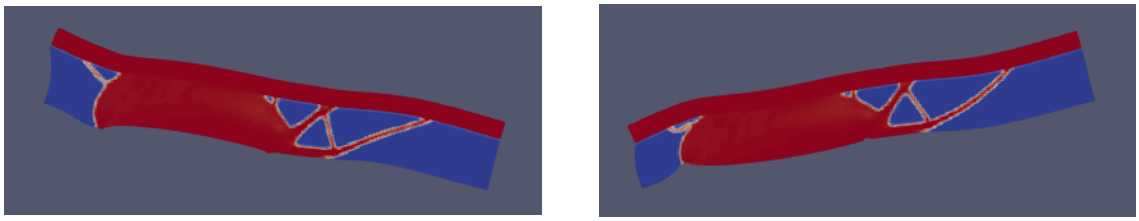

Figure 4.9: Optimized design: motion when excited at $\omega_p = \Omega_4$

The original (benchmark) and the optimized design of the structure can be seen in Figure 4.7. The optimized design was observed to have thicker branches on the right side of the structure to impart greater stability at the top surface. Also, the disappearance of trusses on the left side of the structure could be attributed to a reduction in contractions in that region to keep the top surface flat. The benchmark design structure (Figure 4.8) and the optimized structure when excited at $\omega_p = \Omega_4$ (Figure 4.9) exhibit motion as shown. The top surface could be observed to remain flat as the structure undergoes deformation. The flatness of the surface could be improved by choosing much stricter values of α.

4.4 Discussion

Figure 4.10a shows the FRF of the benchmark design (Table 3.1: Case 1, Figure 3.3a) and Figure 4.10b shows the FRF of the optimized design. As can be seen, no peaks are recorded at the optimized eigenfrequency (Ω_4). It seems like the eigenfrequency is transparent; it exists but with no observed influence at FRF.

Let us consider the reduced response expression from the modal decomposition method [37].

$$G_i = \sum_{k=1}^{N} \frac{\mathbf{c}^{\mathrm{T}} \phi_k \phi_k^{\mathrm{T}} \mathbf{b}}{\Omega_k^2 (1 + \iota\eta) - \omega_i^2} \tag{4.16}$$

where N is the total number of modes, and other terms are as described earlier in subsection 2.5. The structure's response at the 4^{th} eigenfrequency can be expressed as a sum of contributions from individual eigenmodes.

$$G_4 = \sum_{k=1}^{N} \frac{\mathbf{c}^{\mathrm{T}} \phi_k \phi_k^{\mathrm{T}} \mathbf{b}}{\Omega_k^2 (1 + \iota\eta) - \Omega_4^2} \tag{4.17}$$

As discussed above, the structure's response is not affected by the contribution of 4^{th} eigenmode. In other words, the contribution of the 4^{th} eigenmode on the structure's response at 4^{th} eigenfrequency is close to zero.

$$\frac{\mathbf{c}^{\mathrm{T}} \phi_k \phi_k^{\mathrm{T}} \mathbf{b}}{\iota\eta\Omega_4^2} \approx 0 \tag{4.18}$$

The numerator ($\mathbf{c}^{\mathrm{T}} \phi_k \phi_k^{\mathrm{T}} \mathbf{b}$) of this term is called Modal Participation Factor (MPF). The MPF determines how dominantly a given eigenmode contributes to the dynamic response of the structure. Modes with higher MPF get the most excited and largely determine the structural response at a particular operational frequency.

$$\begin{aligned} \mathbf{c}^{\mathrm{T}} \phi_k \phi_k^{\mathrm{T}} \mathbf{b} &\approx 0 \\ \therefore \quad \mathbf{c}^{\mathrm{T}} \phi_k \approx 0 \quad \text{and/or} \quad \phi_k^{\mathrm{T}} \mathbf{b} &\approx 0 \end{aligned} \tag{4.19}$$

This shows that the input and output forces are decoupled and orthogonal to each other. In other words, the input force does not excite the subject eigenmode (i.e., the 4^{th} eigenmode), therefore not causing any output displacement.

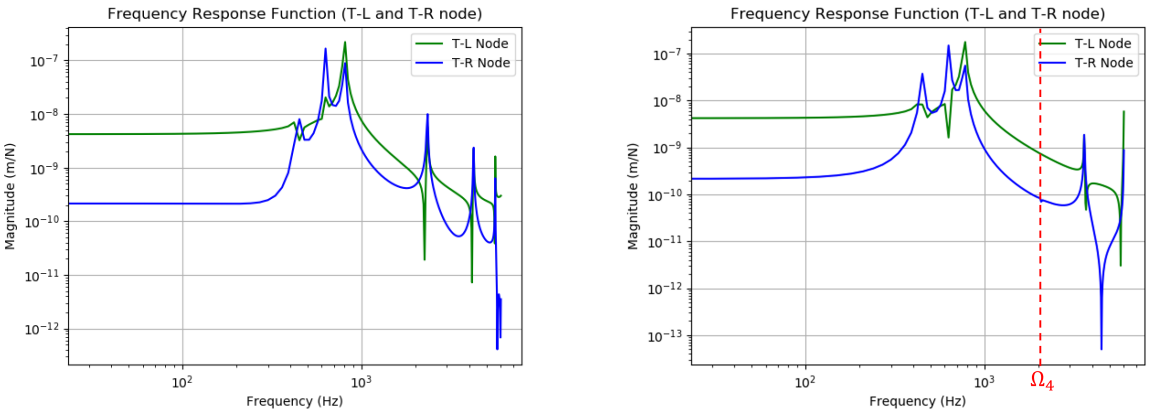

(a) Benchmark design (Case 1)

(b) Optimized design (Case 3)

Figure 4.10: Comparison of FRFs of structure (Table 4.1)

Table 4.1: Results: Dynamic Global Flatness

Case	**Case 1**	**Case 2**	**Case 3**	**Case 4**
Operating frequency (ω_p)		3000 Hz	Ω_4	Ω_4, Ω_5
Constraints	No constraints	$g_{\text{fit}} \leq \alpha$	$g_{\text{fit}} \leq \alpha$ $g_{\text{phase}} \leq \gamma$	$g_{\text{fit}} \leq \alpha$ $g_{\text{phase}} \leq \gamma$
Maximum deviation				
@ $\omega_p = 3000$Hz	0.45 nm N^{-1}	0.36 nm N^{-1} ↓	-	-
@ $\omega_p = \Omega_4$	89.76 nm N^{-1}	-	0.80 nm N^{-1} ↓	0.82 nm N^{-1} ↓
Ω_1	440 Hz	438 Hz	445 Hz	440 Hz
MPF	-0.002431	-0.004674 ↑	-0.006044 ↑	-0.005762 ↑
Ω_2	627 Hz	628 Hz	633 Hz	631 Hz
MPF	0.027378	0.026385 ↓	0.030387 ↑	0.028129 ↑
Ω_3	802 Hz	778 Hz	776 Hz	772 Hz
MPF	-0.044327	-0.031090 ↓	-0.032179 ↓	-0.029659 ↓
Ω_4	2330 Hz	2211 Hz	2172 Hz	1998 Hz
MPF	0.018330	-0.000163 ↓	0.000012 ↓	0.000016 ↓
Ω_5	4220 Hz	3918 Hz	3567 Hz	3483 Hz
MPF	-0.008336	-0.001941 ↓	0.005143 ↓	0.000070 ↓
Ω_6	5576 Hz	5745 Hz	5467 Hz	5624 Hz
MPF	0.001423	0.009876 ↑	0.002984 ↑	0.013019 ↑

The MPF of the first six eigenmodes for different formulations is summarized in Table 4.1. It can be observed that the MPF of Ω_4 for Case 3 and Ω_4, Ω_5 for Case 4, respectively, drop down significantly, demonstrating lower modal participation of those eigenmodes. It can be noticed that the MPF of eigenmodes neighboring to optimizing frequency (operating frequency) decreases while it increases for those farther away. This implies that the imaginary components were optimized to reduce MPF for subject eigenfrequency, while for eigenmodes farther away, the imaginary components increase, increasing their MPF. We can intuit that the imaginary components remain constant for a particular damping model. It can only be optimized to increase/decrease for particular eigenfrequencies, which is then characterized by a corresponding decrease/increase in imaginary components of other eigenfrequencies (depending on the distance from the subject eigenfrequency).

It was also observed that the maximum response peak at the optimized eigenfrequency is considerably reduced (by two orders of magnitude) by implementing global flatness constraints. Thus, response peak minimization can be considered an implicit result of achieving dynamic global flatness. This can be attributed to the fact that to keep the surface flat, the optimizer limits or suppresses vibrations at the top surface by decreasing imaginary components. This method effectively reduces responses at eigenfrequencies that can not be pushed out of the excitation frequency band S_ω.

4.5 Conclusion

This Chapter aimed to develop and investigate the TO approach to ensure the dynamic global flatness of vibrating structures. The results indicate that, indeed, applying a phase constraint to restrict the phase differences between top surface nodes and LSF constraint on real displacement components produced desired results. Some conclusions can be summarized as follows:

1. The response of a structure at eigenfrequency is characterized by huge imaginary components compared to the real components. This results in huge phase differences. Thus, for dynamic flatness, phase difference needs to be constrained along with constraining the shape of the real part.
2. It was observed that the FRFs of the optimized designs showed no peaks at the optimized eigenfrequency. The eigenfrequency seems to exist but has no observed influence on the structure's response. The response is continuous without any disturbances, from the previous eigenfrequency onto the next one. This is because the design is optimized to decouple input and output forces, i.e., input forces have no effect on the structure's response at the subject eigenfrequency, which makes the MPF of that particular eigenmode approximately zero.
3. The maximum response peak at the optimized eigenfrequency was reduced considerably (by two orders of magnitude) by implementing global flatness constraints. This can be attributed to the fact that to keep the surface flat, the optimizer limits or suppresses vibrations at the top surface. This method effectively reduces responses at eigenfrequencies that can not be pushed out of the excitation frequency band S_ω.
4. The phase constraint and LSF constraint in this work has been applied to global flatness problems but may also be used for local flatness problems.

Chapter 5

Case Study

As a typical example of a high-tech application, consider a high precision positioning system. The motion stage must be positioned very precisely with respect to a reference. The working principle of the system is schematically illustrated in Figure 5.1a. The IFM beam is directed to the tilted (45-degree angle) mirror side surface, which enables out-of-plane (z) position measurement. This, however, requires that the IFM beam is returned to the IFM system by a dedicated reference mirror, i.e., the high accuracy positioning apparatus, that is attached to the bottom of the Metro(logy) Frame (MF). The reference mirror is the focus of this case study.

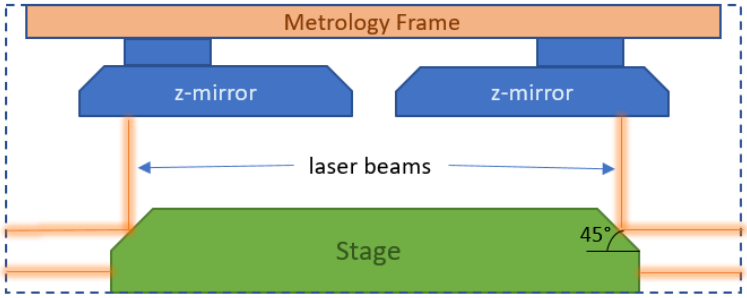

(a) IFM system

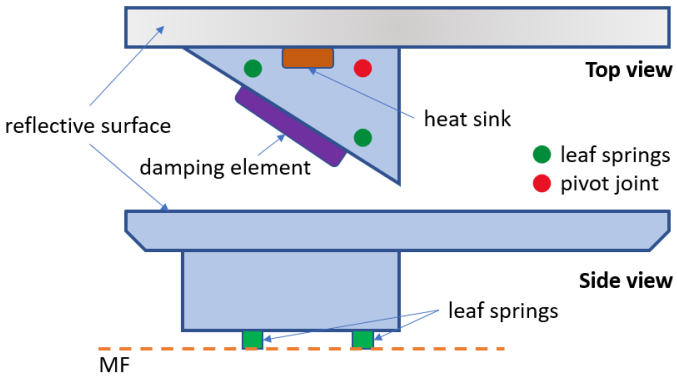

(b) reference mirror assembly

Figure 5.1: Conceptual illustration of IFM system and reference mirror assembly

As shown in Figure 5.1b, the reference mirror is attached to the MF through leaf spring flexures and a pivot joint. A damping element and a heat sink have been assembled with the reference mirror for dynamic and thermal stability. This is a multiple input multiple output (MIMO) case, i.e., several loading factors are present in the system in the form of vibrations from MF and thermal loading effects. The reflective surface of the mirror must remain flat throughout and must not deform. The MF and the reference mirror should, in theory, produce a rigid body. To summarize, the reference mirror must meet strict specifications in terms of static and dynamic qualities, interface connections and stiffnesses, and mechanical stresses caused by temperature variations. This makes the design problem very complex, with multiple objectives and constraints.

5.1 Design Objective

A list of main specifications of reference mirror is given in Table 5.1. A fixed design domain has been given. The position error due to various contributions has been mentioned. This includes the dynamic contribution from vibrations induced by MF onto the reference mirror and thermal contribution from various sources of heat. The global flatness of the entire reflecting surface of the reference mirror must be ensured. Eigenfrequency limits have also been given to avoid natural frequencies of the reference mirror from lying in the frequency bands of incident excitation frequencies.

S. No.	Specification
1	Position error due to reference mirror displacement w.r.t MF (nm)
1.1	Dynamics contribution (nm)
1.2	Thermal contribution (nm)
2	Global flatness (residual after fit in nm)
3	Eigenfrequency limits (Hz)
4	Functional mirror size (mm)

Table 5.1: Main specifications of reference mirror

5.2 Preliminary results

The 3D design model for the reference mirror for TO is shown in Figure 5.2. The top layer of the reflecting surface (red region) is modeled as a non-design layer with a density one since we want that domain to be completely solid to prevent deformations. The design domain is depicted in the grey region, while the blue region depicts void areas. The stiffness of interface connections, i.e., leaf springs and pivot joint, is modeled as per the given system. The first eight eigenmodes of the model are shown in Figure 5.3.

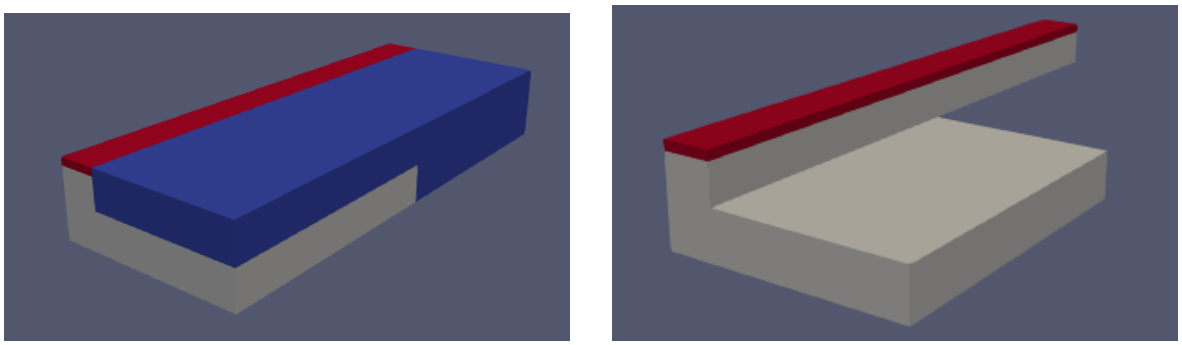

Figure 5.2: 3D model for TO of reference mirror

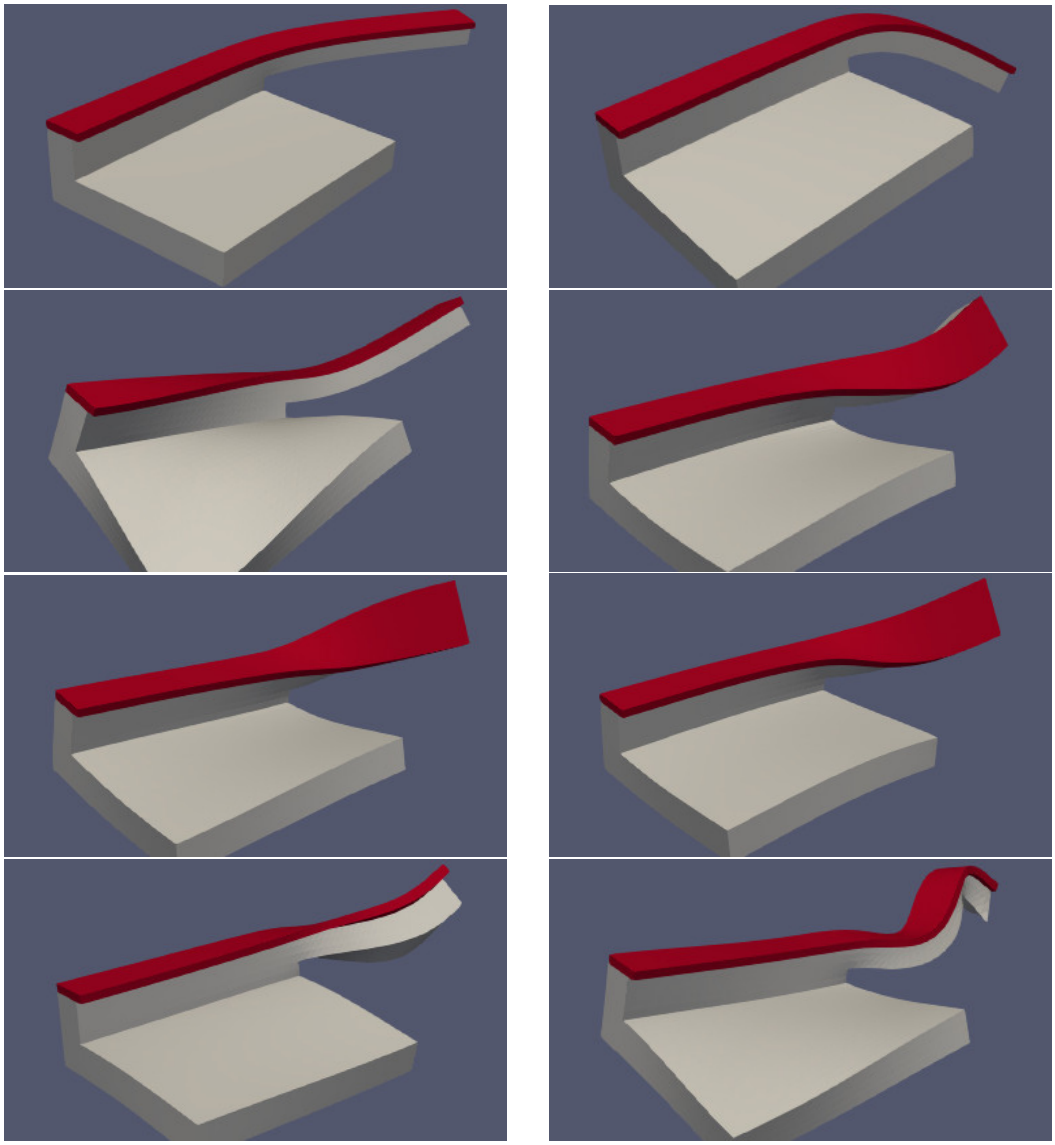

Figure 5.3: Eigenmodes of model (L-R: 1^{st} to 8^{th})

Eigenfrequency maximization:

$$\min_{\mathbf{s}} \quad \left(\sum_{i=1}^{n} \frac{1}{\Omega_i(\mathbf{s})} \right) \qquad V_f \geq 0.5 \tag{5.1}$$

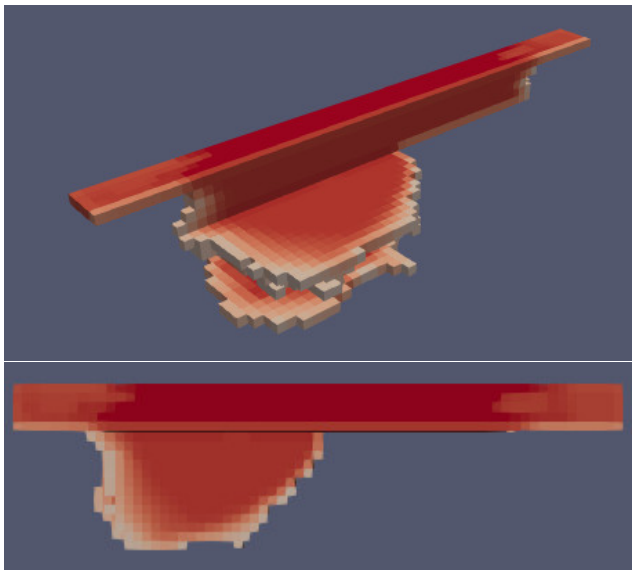

Figure 5.4: Optimized design for eigenfrequency maximization

Eigenfrequency maximization with *p-norm* peak constraint for all nodes at top surface:

$$\begin{aligned} \min_{\mathbf{s}} \quad & \left(\sum_{i=1}^{n} \frac{1}{\Omega_i(\mathbf{s})} \right) \\ \text{s.t.} \quad & G_{\text{top,max}}(\omega_p, \mathbf{s}) \leq g_{\text{upp}}(\omega_p) \\ & V_f \geq 0.5 \end{aligned} \tag{5.2}$$

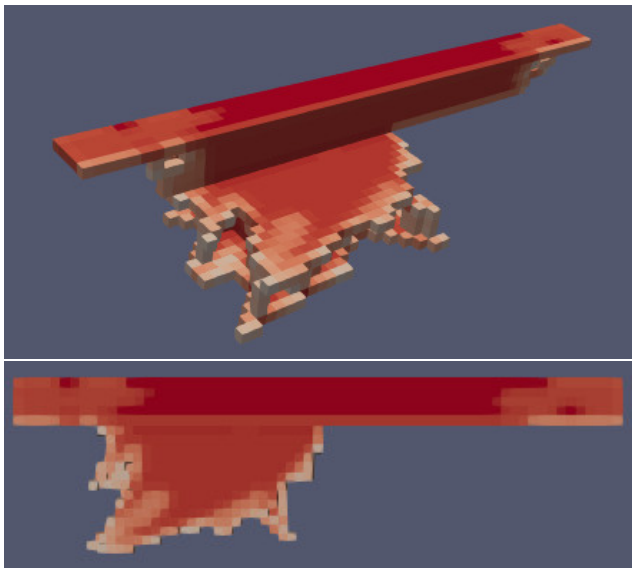

Figure 5.5: Optimized design for eigenfrequency maximization with *p-norm* peak constraint for all nodes at top surface

Chapter 6

Closure

6.1 Conclusion

The aim of this study was to develop and investigate TO methods for the suppression of vibrations on the surface of a suspended structure and achieving dynamic flatness globally on the surface. A non-collocated I/O system with suspended springs was modeled in TO framework, and possible objective functions and constraint functions were analyzed. With the research presented, some inferences can be drawn out.

The influence of suspension modes and flexible modes on the objective function was inspected. Suspension modes need to be included to ensure the formation of structure relevant to boundary conditions, while flexible modes can be chosen based on the highest frequency bands of excitations. Also, the inclusion of suspension modes in the objective function compels the optimizer to push towards lower volume structures. Thus, weight minimization is implicitly achieved in the mean eigenvalue objective function. Volume fraction constraints can be incorporated in the formulation as per requirements.

Aggregating response peaks at a single frequency in spatial domain using *p-norm* function proved very effective and efficient. Aggregation reduced computational times by 47% for four peaks and approximated 98% for 261 peaks as per our model. On the other hand, aggregation of peaks in the frequency domain using *p-norm* function was proved infeasible. Frequency is fundamentally different from space which makes it difficult for aggregation. When frequency response peaks are aggregated using *p-norm* function, the optimizer compels eigenfrequencies lying in the frequency band to approach the subject frequencies, which are marked with convergence issues. Though, aggregating resonant peaks using *p-norm* function is quite feasible where convergence issues are avoided. To optimize responses at frequencies lying in a frequency band, it is efficient and effective to apply transfer function constraints at lower and upper limits of the frequency band and constrain the subject eigenfrequencies to avoid them from lying in the frequency band.

For wider frequency bands where it is infeasible to push eigenfrequencies out of the bands, the response at the eigenfrequency of a structure is inspected. The resonant response of a structure is characterized by huge imaginary components as compared to the real components. The imaginary parts can be constrained, which reduces the response of the structure and also aids in achieving dynamic flatness. With the incorporation of the phase constraint on the top layer and constraining the shape of the real parts of displacements by the least squares fit function, the dynamic global flatness of a suspended surface experiencing vibrations can be obtained. The maximum response peak at the optimized eigenfrequency was reduced considerably (by two orders of magnitude) by implementing phase and LSF constraints. The MPF factor of the subject eigenfrequency reduced considerably to approximately zero. This is because the design is optimized to decouple input and output forces, i.e., input forces have no effect on the response of the structure at the subject

eigenfrequency. The phase constraint and LSF constraint in this work has been applied to global flatness problems but may well be used for local flatness problems too.

6.2 Recommendations

Looking forward, there are several interesting research topics that may serve as extensions to work presented in this thesis:

- Using mean-eigenvalue as an objective function poses some complexities with regard to flexibility in the optimization of a particular eigenfrequency. Frequency response constraints might compel the optimizer to lower a particular eigenfrequency while the mean eigenvalue objective function acts opposite by increasing eigenfrequencies. Alternate objective functions could be implemented to better suit the requirements as per application.
- For the aggregation of peaks using *p-norm* function, using higher values of p improves the accuracy of the approximation. This decreases the accuracy of sensitivities since the resulting function is not smooth anymore, which leads to oscillations in optimized designs. It might be interesting to look at the sensitivities of the sensitivities of *p-norm* function to establish a robust framework for choosing the value of p maintaining a balance between the accuracy of approximations and sensitivities.
- Response at the eigenfrequency of the structure highly depends on the type of damping model implemented. As per requirements, improved damping models may be implemented to improve the accuracy of results. Some recommended damping models are Rayleigh damping and Voigt / Maxwell damping models [38].
- The thickness of the non-design layer can be optimized to obtain optimal damping at the top layer as per design specifications. Related to this, a damping material can also be modeled in the design domain to improve response in a peak limitation context. Effective material placement with different damping properties can be used to obtain much improved results [39, 40].
- Formulations for dynamic global flatness in this work focus on optimizing the phase of all nodes at the top surface to $180°$ or $-180°$. More advanced formulations may be worked out where deviation in phase difference between nodes is restricted to ensure synchronization.
- Formulations for dynamic global flatness can be extended to incorporate surface straightness (2D) or surface parallelism (3D), i.e., to optimize for the suspended structure's top surface to stay parallel to the base. This could be utilized for designing wafer table tops that are subjected to vibrational disturbances and must remain flat for efficient functioning.

Bibliography

[1] Chunchuan Liu et al. "Recent advances in micro-vibration isolation". In: *Mechanical Systems and Signal Processing* 56 (May 2015), pp. 55–80. ISSN: 10961216. DOI: 10.1016/j.ymssp.2014.10.007.

[2] Bo Yan et al. "Self-Sensing Electromagnetic Transducer for Vibration Control of Space Antenna Reflector". In: *IEEE/ASME Transactions on Mechatronics* 22 (5 Oct. 2017), pp. 1944–1951. ISSN: 10834435. DOI: 10.1109/TMECH.2017.2712718.

[3] J. D. Yau and Y. B. Yang. "Vibration reduction for cable-stayed bridges traveled by high-speed trains". In: *Finite Elements in Analysis and Design* 40 (3 Jan. 2004), pp. 341–359. ISSN: 0168874X. DOI: 10.1016/S0168-874X(03)00051-9.

[4] Dao Gong, Jin Song Zhou, and Wen Jing Sun. "On the resonant vibration of a flexible railway car body and its suppression with a dynamic vibration absorber". In: *JVC/Journal of Vibration and Control* 19 (5 Apr. 2013), pp. 649–657. ISSN: 10775463. DOI: 10.1177/1077546312437435.

[5] Lin Li et al. "Micro-vibration suppression methods and key technologies for high-precision space optical instruments". In: *Acta Astronautica* 180 (Mar. 2021), pp. 417–428. ISSN: 00945765. DOI: 10.1016/j.actaastro.2020.12.054.

[6] Makoto Iwasaki, Kenta Seki, and Yoshihiro Maeda. "High-precision motion control techniques: A promising approach to improving motion performance". In: *IEEE Industrial Electronics Magazine* 6 (1 Mar. 2012), pp. 32–40. ISSN: 19324529. DOI: 10.1109/MIE.2012.2182859.

[7] Bendsoe. "Structural Optimization Optimal shape design as a material distribution problem". In: *Structural Optimization* 1 (1989), pp. 193–202.

[8] Niels Olhoff and Jianbin Du. "Topological design of freely vibrating continuum structures for maximum values of simple and multiple eigenfrequencies and frequency gaps". In: (2007). DOI: 10.1007/s00158-007-0101-y.

[9] Jensen and Pedersen. "On maximal eigenfrequency separation in two-material structures: The 1D and 2D scalar cases". In: *Journal of Sound and Vibration* 289 (4-5 Feb. 2006), pp. 967–986. ISSN: 10958568. DOI: 10.1016/j.jsv.2005.03.028.

[10] Niels Olhoff and Jianbin Du. "On Structural Topology Optimization Against Vibration and Noise". In: (2009).

[11] Ma, Cheng, and Kikuchi. "Structural design for obtaining desired eigenfrequencies by using the topology and shape optimization method". In: *Systems in Engineering* 5 (1994), pp. 77–89.

[12] Sajjad Zargham et al. "Topology optimization: a review for structural designs under vibration problems". In: *Structural and Multidisciplinary Optimization* 53 (6 June 2016), pp. 1157–1177. ISSN: 16151488. DOI: 10.1007/s00158-015-1370-5.

[13] Z.-D Ma, N Kikuchi, and I Hagiwara. *Structural topology and shape optimization for a frequency response problem*. 1993, pp. 157–174.

[14] Jog. "Topology design of structures subjected to periodic loading". In: *Journal of Sound and Vibration* 253 (3 June 2002), pp. 687–709. ISSN: 0022460X. DOI: 10.1006/jsvi.2001.4075.

[15] Niels Olhoff and Jianbin Du. "Topological design of continuum structures subjected to forced vibration". In: (2005).

[16] Niels Olhoff and Jianbin Du. "Topological design for minimum dynamic compliance of structures under forced vibration". In: *CISM International Centre for Mechanical Sciences, Courses and Lectures* 549 (2014), pp. 325–339. ISSN: 23093706. DOI: 10.1007/978-3-7091-1643-2_13.

[17] Niels Olhoff and Jianbin Du. "Generalized incremental frequency method for topological designof continuum structures for minimum dynamic compliance subject to forced vibration at a prescribed low or high value of the excitation frequency". In: *Structural and Multidisciplinary Optimization* 54 (5 2016), pp. 1113–1141. ISSN: 16151488. DOI: 10.1007/s00158-016-1574-3.

[18] Lars Krog and Niels Olhoff. "Optimum topology and reinforcement design of disk and plate structures with multiple stiffness and eigenfrequency objectives". In: (1998).

[19] Zhen Luo, Jingzhou Yang, and Liping Chen. "A new procedure for aerodynamic missile designs using topological optimization approach of continuum structures". In: *Aerospace Science and Technology* 10 (2006), pp. 364–373. DOI: 10.1016/j.ast.2005.12.006.

[20] Olavo Silva, Miguel Neves, and Arcanjo Lenzi. "A critical analysis of using the dynamic compliance as objective function in topology optimization of one-material structures considering steady-state forced vibration problems". In: *Journal of Sound and Vibration* 444 (Mar. 2019), pp. 1–20. ISSN: 10958568. DOI: 10.1016/j.jsv.2018.12.030.

[21] Frédéric Bosché and Emeline Guenet. "Automating surface flatness control using terrestrial laser scanning and building information models". In: *Automation in Construction* 44 (2014), pp. 212–226. ISSN: 09265805. DOI: 10.1016/j.autcon.2014.03.028.

[22] Guchuan Zhu et al. "Flatness-based control of electrostatically actuated MEMS with application to adaptive optics: A simulation study". In: *Journal of Microelectromechanical Systems* 15 (5 Oct. 2006), pp. 1165–1174. ISSN: 10577157. DOI: 10.1109/JMEMS.2006.880198.

[23] Steven A Cornelissen et al. *MEMS Deformable Mirrors for Adaptive Optics in Astronomical Imaging*. 2010.

[24] Bendsoe and Sigmund. *Topology Optimization Theory Methods and Applications*. 2003.

[25] M Zhou and G I N Rozvany. *The COC algorithm, Part II: Topological, geometrical and generalized shape optimization*. 1991, pp. 309–336.

[26] Jihong Zhu, Weihong Zhang, and Pierre Beckers. "Integrated layout design of multi-component system". In: *International Journal for Numerical Methods in Engineering* 78 (6 May 2009), pp. 631–651. ISSN: 00295981. DOI: 10.1002/nme.2499.

[27] Svanberg. "Method of Moving Asymptotes". In: *International Journal for Numerical Methods in Engineering* 24 (1987), pp. 359–373.

[28] Tyler E Bruns and Daniel A Tortorelli. *Topology optimization of non-linear elastic structures and compliant mechanisms*. 2001.

[29] R. R. Craig and A. J. Kurdila. *Fundamentals of Structural Dynamics*. 2006. ISBN: 9786468600.

[30] Schmidt et al. *The Design of High Performance Mechatronics*. 2014, pp. 2020–2031.

[31] P. Duysinx and O. Sigmund. "New developments in handling stress constraints in optimal material distribution". In: *7th AIAA/USAF/NASA/ISSMO Symposium on Multidisciplinary Analysis and Optimization* (1998), pp. 1501–1509. DOI: 10.2514/6.1998-4906.

[32] Eduardo Fernández et al. "An aggregation strategy of maximum size constraints in density-based topology optimization". In: *Structural and Multidisciplinary Optimization* 60 (5 Nov. 2019), pp. 2113–2130. ISSN: 16151488. DOI: 10.1007/s00158-019-02313-8.

[33] Y. Maeda et al. “Structural topology optimization of vibrating structures with specified eigenfrequencies and eigenmode shapes”. In: *International Journal for Numerical Methods in Engineering* 67 (5 July 2006), pp. 597–628. ISSN: 00295981. DOI: 10.1002/nme.1626.

[34] T. D. Tsai and C. C. Cheng. “Structural design for desired eigenfrequencies and mode shapes using topology optimization”. In: *Structural and Multidisciplinary Optimization* 47 (5 May 2013), pp. 673–686. ISSN: 1615147X. DOI: 10.1007/s00158-012-0840-2.

[35] Wilfredo Rubio et al. “Tailoring vibration mode shapes using topology optimization and functionally graded material concepts”. In: (2011). DOI: 10.1088/0964-1726/20/2/025009.

[36] Ake Bjorck. *Least Squares Methods*. 1990.

[37] Gil Yoon. “Structural topology optimization for frequency response problem using model reduction schemes”. In: *Computer Methods in Applied Mechanics and Engineering* 199 (25-28 May 2010), pp. 1744–1763. ISSN: 00457825. DOI: 10.1016/j.cma.2010.02.002.

[38] Sondipon Adhikari. *Damping Models for Structural Vibration*. 2000.

[39] Akihiro Takezawa et al. “Topology optimization of damping material for reducing resonance response based on complex dynamic compliance”. In: *Journal of Sound and Vibration* 365 (Mar. 2016), pp. 230–243. ISSN: 10958568. DOI: 10.1016/j.jsv.2015.11.045.

[40] Zhan Kang et al. “On topology optimization of damping layer in shell structures under harmonic excitations”. In: *Structural and Multidisciplinary Optimization* 46 (1 July 2012), pp. 51–67. ISSN: 1615147X. DOI: 10.1007/s00158-011-0746-4.

Appendix A

Eigenfrequency validation

Consider the model mesh shown in Figure 2.2b. The first flexible eigenfrequency of the structure (Figure A.1) was validated through analytical calculations. The eigenfrequency of a simply supported beam is as follows:

$$\Omega_1 = \frac{\pi^2}{l^2}\sqrt{\frac{EI}{m}} \tag{A.1}$$

where E is the Young's modulus, I is the second moment of area or the area moment of inertia, and m is the mass per unit length of the beam. I and m can be calculated as follows:

$$\begin{aligned} I &= \frac{bh^3}{12} \\ m &= \frac{\rho V}{l} = \rho\frac{lbh}{l} = \rho bh \end{aligned} \tag{A.2}$$

The values of E and ρ are defined in Table 2.1. Values of l, b and h are defined in the model mesh.

Analytically calculated Ω_1 = 6703 Hz

Python model (V_f = 1) Ω_1 = 6479 Hz

Error = 3.46 %

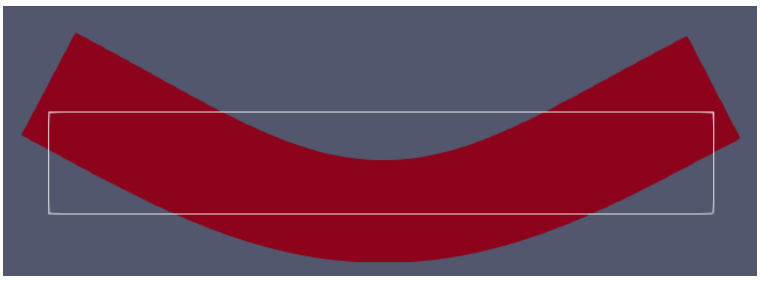

Figure A.1: First eigenmode of the model (V_f = 1)

Appendix B

Influence of suspension and flexible eigenmodes on mean-eigenvalue

Influence of suspension modes and flexible eigenmodes on the structure formation was investigated when mean-eigenvalue is implemented as the objective function. Table B.1 shows the different formulations and Figure B.1 shows the optimized designs as obtained.

Table B.1: Optimization formulations: influence of suspension and flexible eigenmodes on mean-eigenvalue

Case	Objective	Volume	Ω_1	Ω_2	Ω_3	Ω_4	Ω_5	Ω_6
	Ω_{initial} (itr. 1)	$V_{f,\text{initial}} = 0.50$	315 Hz	554 Hz	797 Hz	1560 Hz	3304 Hz	5267 Hz
1	$\sum_{i=1}^{3} \frac{1}{\Omega_i}$	$0.50 < V_f < 0.55$	449 Hz	642 Hz	832 Hz	1970 Hz	3168 Hz	4346 Hz
		% increase	43%	16%	04%	26%	-04%	-18%
2	$\sum_{i=4}^{6} \frac{1}{\Omega_i}$	$0.50 < V_f < 0.55$	361 Hz	585 Hz	768 Hz	3118 Hz	5697 Hz	8140 Hz
		% increase	34%	15%	-04%	100%	72%	55%
3	$\sum_{i=1}^{6} \frac{1}{\Omega_i}$	$0.50 < V_f < 0.55$	448 Hz	643 Hz	832 Hz	2309 Hz	3690 Hz	5212 Hz
		% increase	39%	13%	01%	46%	22%	07%

Some observations are listed below:

1. Lower V_f constraint is active for optimizations involving suspension modes since eigenfrequencies of these suspension modes is inversely proportional to the mass of the structure.
2. Upper V_f constraint is active when only flexible eigenmodes are included in the mean-eigenvalue objective function. This is because with higher V_f, stiffness of structure increases. This increase is comparatively greater than the increase in the mass of the structure (depending on the value of penalty factor in SIMP).

(a) Case 1: Eigenfrequency maximization with only suspension modes

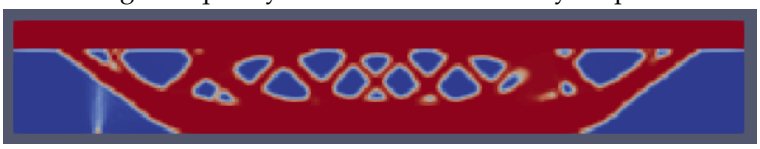

(b) Case 2: Eigenfrequency maximization with only flexible eigenmodes

(c) Case 3: Eigenfrequency maximization with both suspension and flexible eigenmodes

Figure B.1: Optimized designs obtained from formulations shown in Table B.1

3. It can be observed from Figure B.1b that when only flexible eigenmodes are considered in the objective function, a structure is formed in accordance with the eigenmodes considered. However, this structure is irrelevant to the given boundary conditions i.e. interface connections. It can be observed that there is no linkage between the structure and left spring.
4. When suspension modes are included in the objective function, the optimized design formed is very much relevant to the given boundary conditions. Therefore, suspension modes must be included in the mean-eigenvalue objective function to ensure structure formation relevant to boundary conditions. While, the flexible eigenmodes can be included as per the working excitation frequencies system is subjected to.

Appendix C

Multi-objective formulations

Some multi-objective formulations involving mean-eigenvalue and transfer function were implemented and investigated. The multi-objective formulation is as shown below:

$$\begin{aligned} \min_{\mathbf{s}} \quad & \left(\alpha \frac{\text{ef}_{\text{obj}}}{\text{ef}_{\text{initial}}} + \beta \frac{\text{tf}_{\text{obj}}}{\text{tf}_{\text{initial}}} \right) \\ \text{s.t.} \quad & g_{\text{stc}} \leq \gamma \\ & V_f \geq 0.5 \\ & s_{\min} \leq \mathbf{s} \leq 1 \end{aligned} \tag{C.1}$$

where $\text{ef}_{\text{initial}}$ and $\text{tf}_{\text{initial}}$ are 3.91×10^{-7} and 5.13×10^{-11} respectively. Different weighing fractions α and β are chosen as below. g_{stc} is the static compliance constraint where γ is 2×10^{-8}. ef_{obj} and tf_{obj} are as shown below:

$$\begin{aligned} \text{ef}_{\text{obj}} &= \sum_{i=1}^{n} \frac{1}{\Omega_i(\mathbf{s})} \\ \text{tf}_{\text{obj}} &= \left| G_k(\omega_j, \mathbf{s}) \right| \end{aligned} \tag{C.2}$$

Table C.1: Multi-objective formulations: mean-eigenvalue function and transfer function

$\boldsymbol{\alpha}$	$\boldsymbol{\beta}$	$\mathbf{ef_{obj}}$	$\mathbf{tf_{obj}}$
0.1	0.9	2.87×10^{-7}	5.26×10^{-12}
0.2	0.8	2.87×10^{-7}	3.13×10^{-12}
0.3	0.7	2.86×10^{-7}	1.76×10^{-12}
0.4	0.6	2.86×10^{-7}	3.65×10^{-13}
0.5	0.5	2.86×10^{-7}	7.53×10^{-12}
0.6	0.4	2.86×10^{-7}	4.59×10^{-13}
0.7	0.3	2.86×10^{-7}	1.32×10^{-12}
0.8	0.2	2.88×10^{-7}	1.53×10^{-12}
0.9	0.1	2.87×10^{-7}	1.41×10^{-12}

Table C.1 shows final values of ef_{obj} and tf_{obj} as obtained through different multi-objective formulations with varying weighing fractions. Figure C.1 shows resulting optimized designs for different formulations. It was observed that irrespective of weighing fraction α, ef_{obj} saturated to a value of 2.86×10^{-7}. This is because the model was optimized to maximum eigenfrequencies for each case. However, it was observed that using higher values of α promoted structure formation which resulted in better convergence in optimized designs. This is because the tf_{obj} acts against the ef_{obj} and prevents structure formation between I/O points so that deformations can be minimized.

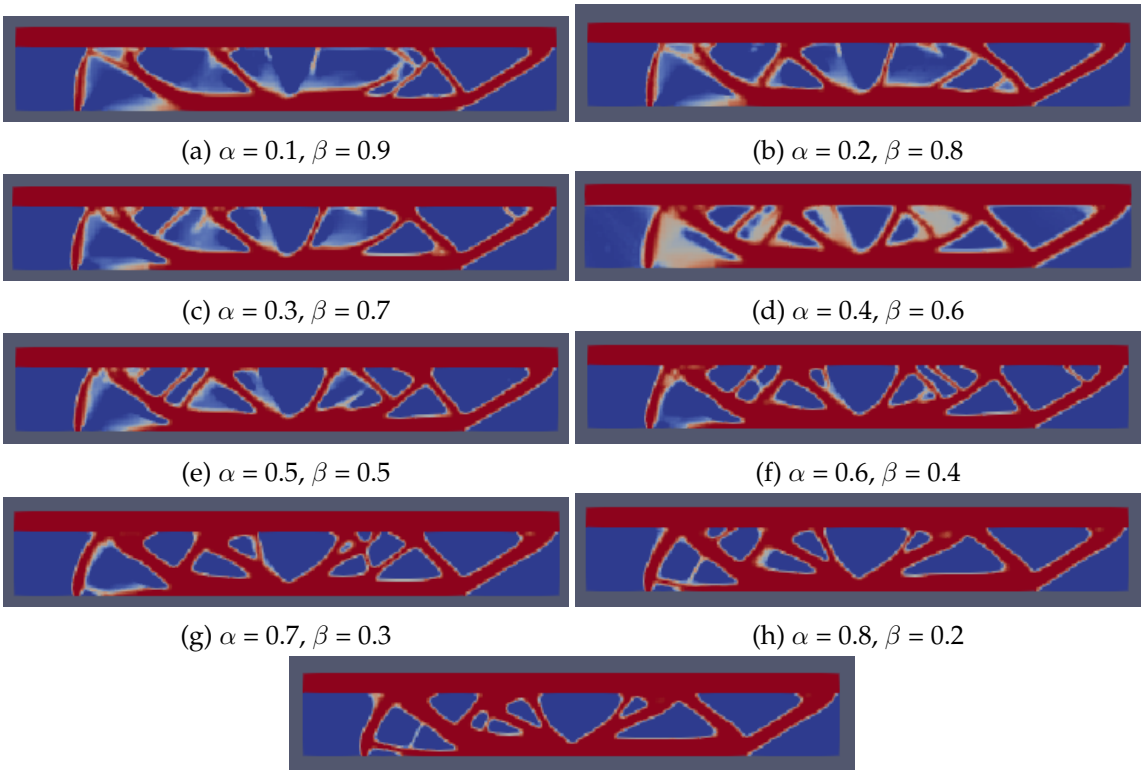

(a) $\alpha = 0.1$, $\beta = 0.9$ (b) $\alpha = 0.2$, $\beta = 0.8$

(c) $\alpha = 0.3$, $\beta = 0.7$ (d) $\alpha = 0.4$, $\beta = 0.6$

(e) $\alpha = 0.5$, $\beta = 0.5$ (f) $\alpha = 0.6$, $\beta = 0.4$

(g) $\alpha = 0.7$, $\beta = 0.3$ (h) $\alpha = 0.8$, $\beta = 0.2$

(i) $\alpha = 0.9$, $\beta = 0.1$

Figure C.1: Optimized designs: multi-objective formulation

Appendix D

Aggregation of resonant peaks using p-norm

Aggregation of resonant peaks using *p-norm* function was investigated. Peaks were initially constrained individually and results were compared after aggregation.

TO formulation for individual constraints:

$$\begin{aligned} \min_{\mathbf{s}} \quad & \left(\sum_{i=1}^{n} \frac{1}{\Omega_i(\mathbf{s})} \right) \\ \text{s.t.} \quad & \left| G_{\text{TR}}(\Omega_j) \right| \leq g_{\text{upp}} \quad \forall \quad j = 4, 5, 6 \end{aligned} \tag{D.1}$$

TO formulation for aggregated constraints:

$$\begin{aligned} \min_{\mathbf{s}} \quad & \left(\sum_{i=1}^{n} \frac{1}{\Omega_i(\mathbf{s})} \right) \\ \text{s.t.} \quad & G_{\text{TR, max}}(\Omega_j) \leq g_{\text{upp}} \quad \forall \quad j = 4, 5, 6 \end{aligned} \tag{D.2}$$

It was observed that aggregation of resonant peaks using *p-norm* function proved to be quite effective. This is because the eigenfrequencies are more flexible to optimize with the absence of operating frequencies from TO formulation. It was observed that computational times of aggregated formulations were similar to those of individual constraints. This is because the number of solutions required for the linear system of equations were same.

(a) Benchmark design

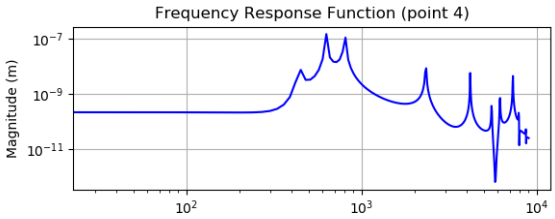

(b) FRF

(c) Individual constraint at TR node at Ω_4

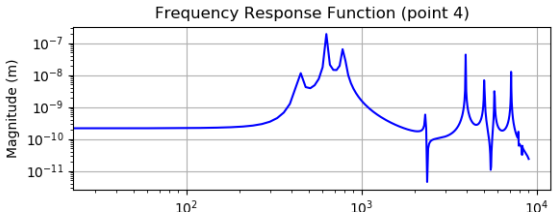

(d) FRF

(e) Individual constraints at TR node at Ω_4, Ω_5

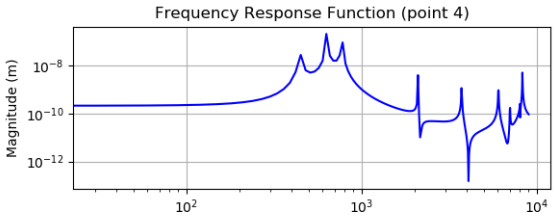

(f) FRF

(g) Individual constraints at TR node at $\Omega_4, \Omega_5, \Omega_6$

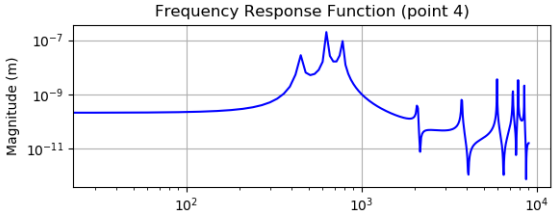

(h) FRF

(i) Aggregated constraint at TR node at $\Omega_4, \Omega_5, \Omega_6$

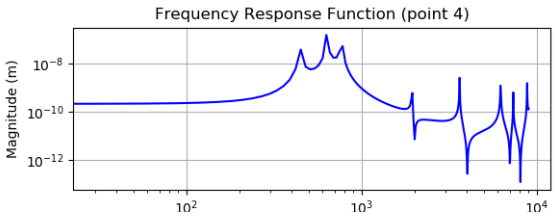

(j) FRF

Figure D.1: Optimized designs and FRF: Aggregation of resonant peaks using p-norm

Appendix E

Peak limitation w.r.t. input spectrum

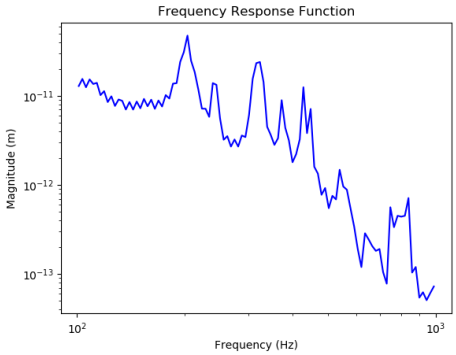

Figure E.1: Input vibrations to a structure

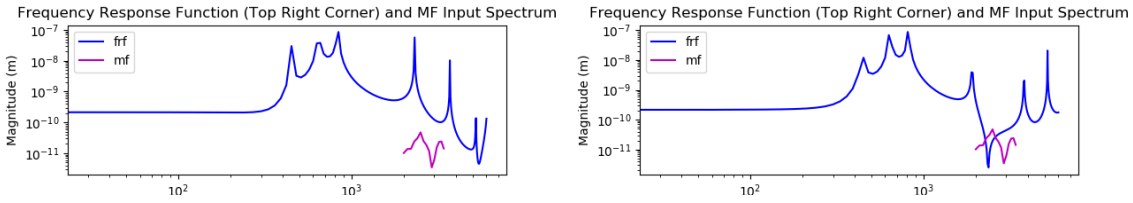

(a) Benchmark design (b) Optimized design w.r.t input spectrum

Figure E.2: Optimizing the FRF of the structure w.r.t. input spectrum

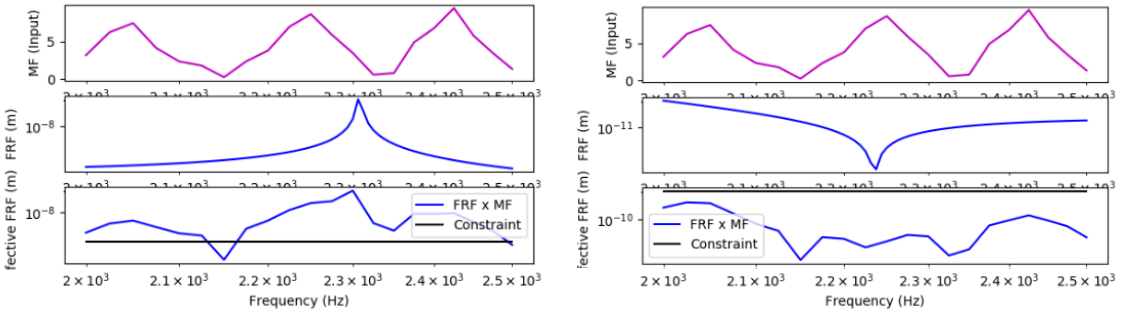

(a) Benchmark design (b) Optimized design w.r.t input spectrum

Figure E.3: Optimizing the FRF of the structure w.r.t. input spectrum - top to bottom: (1) input frequency spectrum, (2) FRF of the structure, (3) Effective FRF of the structure

Appendix F

Global dynamic flatness: random excitation frequency

Global dynamic flatness constraints were applied for a random operational frequency (ω_p = 3000 Hz). The TO formulation is as shown below:

$$\begin{aligned} \min_{\mathbf{s}} \quad & \left(\sum_{i=1}^{n} \frac{1}{\Omega_i(\mathbf{s})} \right) \\ \text{s.t.} \quad & g_{\text{fit}}(\omega_p) \leq \alpha_1 \end{aligned} \tag{F.1}$$

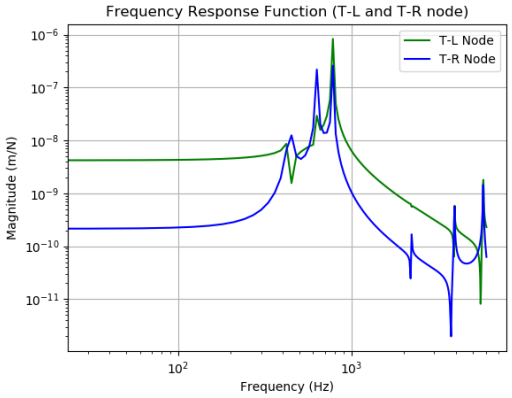

(a) FRF of optimized design

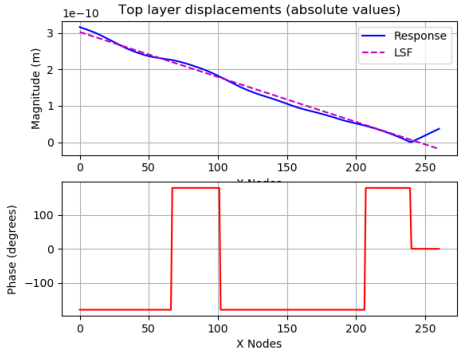

(b) Magnitude and phase of $\mathbf{u}_{\text{top}}$

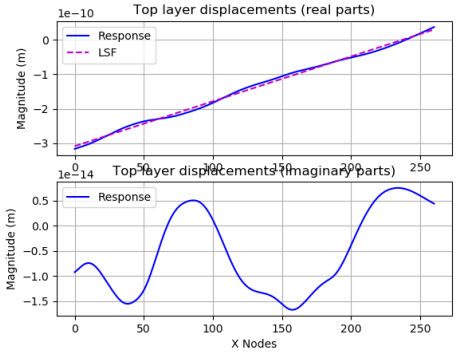

(c) Real and imaginary components of $\mathbf{u}_{\text{top}}$

Figure F.1: Global dynamic flatness at ω_p = 3000 Hz

Appendix G

Global dynamic flatness: two consecutive eigenfrequencies

Global dynamic flatness constraints were applied for two consecutive eigenfrequencies (Ω_4, Ω_5). The TO formulation is as shown below:

$$\begin{aligned} \min_{\mathbf{s}} \quad & \left(\sum_{i=1}^{n} \frac{1}{\Omega_i(\mathbf{s})} \right) \\ \text{s.t.} \quad & g_{\text{fit}}(\Omega_4) \leq \alpha_1 \\ & g_{\text{phase}}(\Omega_4) \leq \gamma_1 \\ & g_{\text{fit}}(\Omega_5) \leq \alpha_2 \\ & g_{\text{phase}}(\Omega_5) \leq \gamma_2 \end{aligned} \tag{G.1}$$

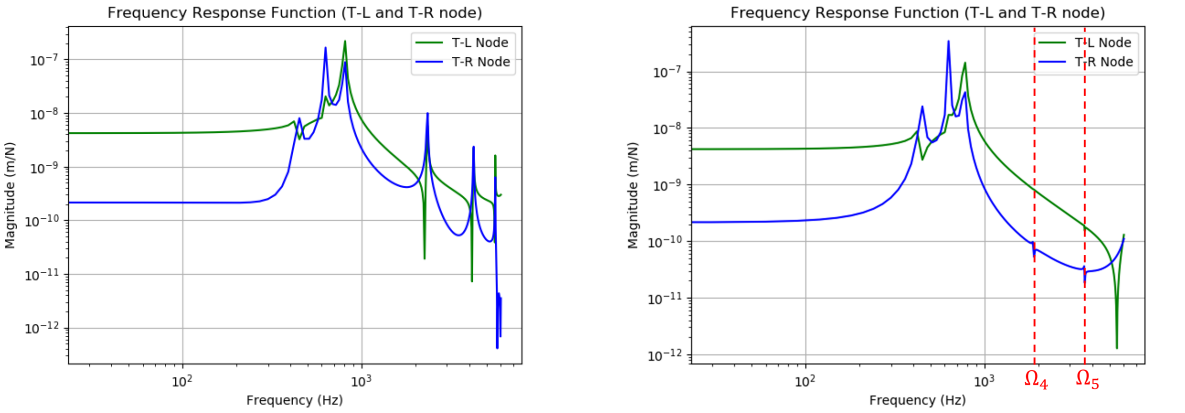

(a) Benchmark design

(b) Optimized design with flatness constraints

Figure G.1: Comparison of FRFs of structure